

1 **Late Ordovician climate change and extinctions driven by elevated volcanic nutrient**  
2 **supply**

3  
4 Jack Longman<sup>1,2,\*</sup>, Benjamin J. W. Mills<sup>3</sup>, Hayley R. Manners<sup>4,5</sup>, Thomas M. Gernon<sup>4</sup> and  
5 Martin R. Palmer<sup>4</sup>

6 <sup>1</sup> Marine Isotope Geochemistry, Institute for Chemistry and Biology of the Marine  
7 Environment (ICBM), University of Oldenburg, PO Box 2503, 26111 Oldenburg, Germany.

8 <sup>2</sup> School of Geography and the Environment, University of Oxford, South Parks Road,  
9 Oxford, OX1 3QY, UK.

10 <sup>3</sup> School of Earth and Environment, University of Leeds, Leeds LS2 9JT, UK.

11 <sup>4</sup> School of Ocean and Earth Sciences, University of Southampton, Southampton, SO14 3ZH,  
12 UK.

13 <sup>5</sup> School of Geography, Earth and Environmental Sciences, University of Plymouth,  
14 Plymouth, PL4 8AA, UK.

15  
16 \*Corresponding Author: [jack.longman@uni-oldenburg.de](mailto:jack.longman@uni-oldenburg.de)

17  
18 **Abstract**

19 **The Late Ordovician (~459–444 million years ago) was characterised by global cooling,**  
20 **glaciation and severe mass extinction. These events may have been driven by increased**  
21 **delivery of the nutrient phosphorus (P) to the ocean, and associated increases in marine**  
22 **productivity, but it is not clear why this occurred in the two pulses identified in the**  
23 **geological record. We link both cooling phases, and the extinction, to volcanic eruptions**  
24 **through marine deposition of nutrient-rich ash and the weathering of terrestrially**  
25 **emplaced ash and lava. We then reconstruct the influence of Late Ordovician volcanic P**  
26 **delivery on the marine system by coupling an estimate of bioavailable phosphate supply**

27 (derived from a depletion and weathering model) to a global biogeochemical model. Our  
28 model compares volcanic ash P content in marine sediments before and after alteration  
29 to determine depletion factors, and we find good agreement with observed carbon  
30 isotope and reconstructed temperature shifts. Hence, massive volcanism can drive  
31 substantial global cooling on million-year timescales due to P delivery associated with  
32 long-term weathering of volcanic deposits, offsetting the transient warming of  
33 greenhouse gas emission associated with volcanic eruptions. Such longer-term cooling  
34 and potential for marine eutrophication may be important for other volcanism-driven  
35 global events.

### 36 Main Text

37 The Late Ordovician mass extinction (LOME) occurred in two phases, and in terms of species  
38 loss was the second greatest extinction event in Earth's history<sup>1-3</sup>. The Late Ordovician is  
39 characterised by a number of carbon isotope excursions (CIEs), with two globally-  
40 represented, the Guttenburg (GICE) at ~454 Ma, and Hirnantian (HICE) at ~ 445 Ma<sup>4</sup>. The  
41 GICE coincides with global cooling, and the beginning of the HICE is associated with  
42 widespread glaciation, with the cooling periods generally implicated in instigating the  
43 LOME<sup>1,5-7</sup>.

44 The primary driver behind the CIEs and associated cooling is uncertain. One  
45 possibility is that the emergence of early nonvascular land plants amplified terrestrial  
46 weathering and increased the delivery of the key limiting nutrient phosphorus to the oceans<sup>8</sup>.  
47 Greater availability of phosphorus increases marine productivity and organic carbon burial,  
48 driving a reduction in atmospheric CO<sub>2</sub> and a positive excursion in carbonate  $\delta^{13}\text{C}$  (ref.<sup>9</sup>).  
49 Other proposals include an increasing fraction of eukaryotic marine production strengthening  
50 the biological pump<sup>10</sup>, and increased tropical weathering resulting from orogenesis  
51 augmenting the supply of phosphorus to the oceans<sup>11</sup>.

52           The concept that Late Ordovician cooling was driven by organic carbon burial is  
53 supported by observations<sup>12</sup>, but why this occurred in two distinct pulses during the GICE and  
54 HICE is unclear. This pulsing may have arisen from early plants colonising new terranes<sup>8</sup>, but  
55 there is little evidence for this, although poor fossil preservation cannot be ruled out<sup>13</sup>.  
56 Further, the pace of early plant evolution remains highly uncertain<sup>13</sup> and there is no evidence  
57 that eukaryotic evolution, or tropical uplift, occurred in distinct pulses. Existing global  
58 biogeochemical models cannot reliably reproduce the Hirnantian glaciation (or isotope  
59 excursions) associated with the HICE when based on known long-term tectonic cycles of  
60 uplift and degassing, and the positioning of the continents<sup>9</sup>, even though these models can  
61 accurately reproduce the Permo-Carboniferous and late Cenozoic icehouses<sup>9</sup>. This suggests  
62 that the Hirnantian icehouse was driven by some climatic forcing mechanism currently not  
63 well-represented in these models.

64           Given the potential association between volcanism and global climate change<sup>14,15</sup>, we  
65 explore the concept that Late Ordovician marine productivity and cooling episodes were  
66 directly related to subaerial volcanic activity. The Late Ordovician was characterised by  
67 extensive volcanic eruptions, preserved in the sedimentary record as bentonites<sup>16,17</sup>. These  
68 bentonites represent some of the largest volcanic eruptions in Earth's history, with estimates  
69 indicating some of the better studied events (Millbrig, Deicke and Kinnekulle) erupted  $\geq 1000$   
70 km<sup>3</sup> of pyroclastic material<sup>18</sup>. In addition, there are hundreds of spatially extensive bentonites  
71 of Late Ordovician (459 – 444 Ma) age preserved across North America<sup>19</sup>, Northern Europe<sup>20</sup>,  
72 and China<sup>16,21</sup>, prompting suggestions of a causal link between volcanism and global cooling  
73 during this period<sup>3,14,17</sup>. Most recently, several studies have employed the total organic carbon  
74 to mercury ratio (TOC/Hg), to directly link volcanic Hg emission to Late Ordovician climatic  
75 change (e.g. refs.<sup>22,23</sup>). However, it remains uncertain whether cooling was driven by rapid  
76 sulfate emissions, through the immediate weathering of ash and lava, or by longer-term

77 weathering of volcanic arcs and uplifted terranes<sup>17,23</sup>, a problem compounded by poorly  
78 constrained volcanic fluxes.

79 Volcanism may cool the climate on non-transitory timescales due to enhanced  
80 productivity and organic carbon preservation<sup>24</sup>, with one of the key drivers being enhanced P  
81 supply derived from leaching of volcanic ash<sup>25</sup>. It is not currently clear how much P may have  
82 been supplied from ash during the Late Ordovician, or how input of volcanic P may have  
83 influenced the marine environment. To answer these questions, we compile global data on P  
84 depletion in tephra layers today, as a method of quantifying P release to the ocean during ash  
85 deposition and diagenesis. We couple our estimates of P flux to a global biogeochemical  
86 model to investigate the potential impact of such nutrient supply to the Late Ordovician  
87 marine carbon cycle.

#### 88 **Timing and extent of volcanism during the Late Ordovician**

89 To estimate timing of volcanic activity, we compile 43 Ar-Ar and U-Pb dates from  
90 North American and Scandinavian bentonites (Fig. 1a), and 24 dates from Chinese bentonites  
91 of Late Ordovician age (Fig. 1b). Our reconstruction indicates that bentonite deposition  
92 occurred in two discrete pulses (Fig. 1c), corresponding to the eruption of two geographically  
93 distinct volcanic provinces (Figure 2). The first pulse represents North  
94 American/Scandinavian volcanism and is well-constrained, with the greatest depositional  
95 intensity occurring between 454.5 – 453 Ma, peaking at 453.5 Ma (Fig. 1c). This peak  
96 primarily represents highly-precise measurements of the North American “big” bentonites,  
97 the Deicke and Millbrig<sup>5,26</sup>, and the Grimstorp bentonite<sup>26</sup>. A slightly earlier peak is also  
98 apparent (c. 456.5 Ma), representing potentially uncertain estimates of the Kinnekulle  
99 bentonite age<sup>27</sup>, and other unnamed bentonites from Oslo<sup>20</sup> (see Supplementary Table 4).  
100 Chinese bentonite ages exhibit more spread, with fewer highly precise dates (Fig. 1c). Our  
101 compilation suggests the most intense volcanism in the China region occurred between 445.25

102 – 442.5 Ma, with a peak at about 444 Ma (Fig. 1c), corresponding to some of the most  
103 accurate dates from outcrop in the south-western Yunnan province<sup>28</sup>, and central Hubei  
104 province<sup>29</sup>. These two volcanic pulses correspond well to the two primary carbon isotope  
105 excursions of the Late Ordovician, the GICE and HICE, and may thus support a link between  
106 volcanism and climate change.

### 107 **P release during ash deposition, diagenesis and weathering**

108 To investigate this hypothesis, we estimate the amount of P which may have been  
109 supplied by the two main pulses of volcanism. To estimate the percentage of P released  
110 during ash deposition and diagenesis, altered ash compositions are compared to unaltered  
111 protolith compositions to estimate metal mobility<sup>30,31</sup>, using protolith data from the GEOROC  
112 database (<http://georoc.mpch-mainz.gwdg.de>) and our data from altered tephras (see  
113 Methods). Specifically, marine sediment-hosted tephras from the Lesser Antilles and the  
114 Aleutian arcs have been analysed and compared to similar data from eight additional modern  
115 volcanic provinces (Fig. 1). In addition to direct input of P from volcanic ash deposition, the  
116 emplacement and subsequent terrestrial weathering of extensive ash beds would have led to a  
117 secondary source of P to the oceans. The scale of this P flux has been estimated from a Monte  
118 Carlo simulation of inputs using published variables including the number, and scale of  
119 eruptions (Methods, Extended Data Figures 1, 2).

120 Depletion factors indicate between 31% (mean) and 48% (median) of the P originally  
121 hosted in tephra is lost during early diagenesis (Fig. 3). The potential scale of this process is  
122 calculated in the modern oceans, using an average of  $1.14 \pm 0.6 \text{ km}^3$  ash deposited per year,  
123 with  $70 \pm 7.5 \%$  falling into the ocean<sup>31</sup>, an ash density of  $1400 \pm 130 \text{ kg/m}^3$  (ref.<sup>32</sup>), and an  
124 original P content in tephra of  $0.41 \pm 0.19 \text{ wt}\%$  (ref.<sup>33</sup>). For each variable, a Monte Carlo-  
125 based approach is applied, using the average and standard deviation to develop 10,000  
126 possible iterations of each variable. From this calculation, the most likely annual P flux from

127 ash deposition and diagenesis is estimated to be approximately  $3 \times 10^{10}$  mol P yr<sup>-1</sup>. This is  
128 similar to estimates of global dust input to the P cycle today ( $3.2 \times 10^{10}$  mol P yr<sup>-1</sup>), and  
129 exceeds the dissolved riverine input ( $0.6 - 1.1 \times 10^{10}$  mol P yr<sup>-1</sup>; ref.<sup>34</sup>). Present-day volcanism  
130 is thought to be far smaller in scale than in periods such as the Ordovician<sup>35,36</sup>. Therefore,  
131 enhanced P supply tied to volcanism likely played an even more important role in  
132 biogeochemical cycles of P during the Ordovician.

### 133 **Impact of volcanic ash supply on Late Ordovician climate**

134 The depletion factors and estimates of ash supply during the Late Ordovician can be  
135 used to quantify the scale of P supply during the two studied events. For the GICE, our  
136 simulations indicate a mean of  $2.29 \times 10^{15}$  mol P (Fig. 4), which increases to  $6.49 \times 10^{15}$  mol  
137 P in the upper estimates of the simulations (95<sup>th</sup> percentile). For the volcanic episode covering  
138 the HICE, our simulations suggest a mean supply of  $2.89 \times 10^{15}$  mol P, with an upper estimate  
139 of  $8.24 \times 10^{15}$  mol P (95<sup>th</sup> percentile) (Fig. 4). In addition to ash falling into the ocean, the  
140 impact of erosion of terrestrially emplaced ash and lava on the P cycle is considered by  
141 estimating weathering fluxes of P (Methods). Newly emplaced ashes and basaltic rocks  
142 weather rapidly<sup>37,38</sup>, such that in Earth's modern configuration, despite representing only 3 –  
143 5% of land area, chemical weathering of basalt contributes ~30% of the total CO<sub>2</sub>  
144 consumption by silicate weathering<sup>37,38</sup>. Our approach to quantifying the impact of this  
145 process results in a mean additional (riverine) P flux from weathering of  $7.51 \times 10^{14}$  mol P  
146 Myr<sup>-1</sup> in the millennia after emplacement (Fig. 4c), with an upper estimate of  $1.23 \times 10^{15}$  mol  
147 P Myr<sup>-1</sup> (95<sup>th</sup> percentile), providing another source of bioavailable P to the ocean system.

148 The impact of this level of volcanic nutrient supply on Ordovician climate is estimated  
149 using the COPSE global biogeochemical model<sup>39</sup>. The GICE and HICE P inputs are  
150 represented by Gaussian functions with their maxima at the times of highest depositional  
151 intensity noted above (i.e., 453.5 and 444 Ma) and with a width of 2 Myrs, constrained in part

152 by the duration of the carbon isotope excursions. The total P input is calculated for both the  
153 means and 95<sup>th</sup> percentiles and is summed from the P depletion model and weathering inputs.  
154 A further factor is also added into the P delivery calculation to represent the recycling of P  
155 from sediments, because P loading and eutrophication in marginal settings leads to a  
156 substantial recycling flux of P from the sediments<sup>40</sup>, due to the increase in anaerobic  
157 processing of organic matter and the scarcity of Fe(III) phases that scavenge P. The COPSE  
158 model does not represent these feedbacks well, because it has a well-mixed global ocean and  
159 no consideration of continental margins, with substantial recycling of P relying on  
160 eutrophication of the global ocean rather than productive shelves and slope environments  
161 alone<sup>39</sup>. This is relevant to the Ordovician, a time when sea level was perhaps 300 m higher  
162 than present<sup>41</sup>, with extensive shelf environments<sup>42</sup>. Hence, parallel experiments were run to  
163 determine the degree to which P recycling is dampened in COPSE versus a published P cycle  
164 model in which the shelves are considered separately (see Methods, ref.<sup>43</sup>). We conclude that  
165 a 5-fold larger P input is required in COPSE to produce the same spike in marine P  
166 concentration observed in the multi-box model (Extended Data Figure 3). Thus, P inputs in  
167 the additional COPSE simulations are increased 5-fold to represent both the initial input and  
168 the additional recycling of P. The large size of this factor is related to the relatively small size  
169 of the ocean shelves (as a fraction of the whole ocean) compared to their disproportionately  
170 large contribution to organic matter burial.

171 An important parameter in COPSE is the degree to which land plants amplify  
172 continental weathering rates. This value is poorly constrained and is typically varied in  
173 sensitivity analyses between around 2- and 7-fold, giving a wide range of possible  
174 background CO<sub>2</sub> concentrations for the early Palaeozoic<sup>44</sup>. We choose a factor 2 enhancement  
175 for the model runs in this work, which gives a relatively low background Ordovician CO<sub>2</sub>  
176 concentration of around 1000 ppm, consistent with more recent proxy data<sup>45</sup>. Other than the  
177 new P inputs and choice of biotic weathering parameter, the model remains identical to the

178 long-term baseline shown in ref.<sup>39</sup>. Figure 5 shows the model outputs for atmospheric CO<sub>2</sub>,  
179 average surface temperature, marine anoxia, and the δ<sup>13</sup>C of new sedimentary carbonates. The  
180 model outputs show that the P release from volcanic ash deposition and weathering, combined  
181 with the recycling of P from sediments, is sufficient to cause large-scale changes in climate  
182 and biogeochemistry as observed in the geological record<sup>10,14</sup>. In the “95<sup>th</sup> percentile +  
183 recycling” input scenario, carbon isotope excursions of ~3‰ and ~4‰ are predicted, which  
184 are synchronous with the GICE and HICE, respectively, and are of similar magnitude. In this  
185 scenario, maximum global cooling at the HICE is around 3°C, and a global average surface  
186 temperature of below 15°C is reached at the nadir. These temperature predictions are in line  
187 with clumped isotope thermometry which suggests the Hirnantian icehouse was relatively  
188 short lived and represented a similar global average temperature to recent Pleistocene  
189 glaciation<sup>6,46</sup>.

190         The extent of marine anoxia increases during the P input events in the model, although  
191 given the global well-mixed ocean in the model, shelf anoxia would be expected to increase  
192 by a larger fraction than the global ocean. This is against a backdrop of marine oxygenation  
193 through the Ordovician and Silurian predicted by COPSE<sup>39</sup>. One of the major features of the  
194 HICE in the geological record is the widespread formation of organic-rich shales, in particular  
195 in China<sup>47,48</sup>, potentially linked to widespread ocean anoxia<sup>10,49</sup>. In COPSE, the relative  
196 increase in anoxia is much larger during the HICE – close to a doubling in the “95<sup>th</sup> percentile  
197 + recycling” scenario.

## 198 **Implications for the LOME**

199         Our model results suggest that volcanic ash diagenesis and weathering of erupted  
200 products likely played a key role in the Late Ordovician Earth system. In order to reproduce  
201 the magnitude of Earth system change, we require that these inputs are at the 95<sup>th</sup> percentile of  
202 our analysis. However, given the relatively sparse nature of the geological record of the



203 Palaeozoic, and the conservative approach utilised here to derive estimates of P supply from  
204 ash (Methods), we stress that our analysis likely underestimates the number of volcanic  
205 events. This is supported by the close comparison between the model output of the “95th  
206 percentile + recycling” input scenario and proxy data (Fig. 5, ref.<sup>50</sup>). Our results may explain  
207 several features of the LOME, which do not follow trends associated with other mass  
208 extinctions, in particular their link to cooling, rather than warming. Volcanic activity has been  
209 invoked as the driver behind a number of short-term climatic upheavals and mass  
210 extinctions<sup>51</sup>, including those at the end of the Permian<sup>52</sup> and in the Triassic periods<sup>53</sup>,  
211 resulting in the rapid fluctuations between icehouse and greenhouse conditions known to  
212 stress faunas and drive biodiversity loss<sup>3,52</sup>.

213 For the Late Ordovician, it appears that the long-term nature of nutrient supply from  
214 weathering of eruptive products such as volcanic ash plays a more dominant role than the  
215 medium-term warming associated with CO<sub>2</sub> injection. When comparing to climatic change, it  
216 is clear that the first stepped decrease in faunal diversity occurred soon after the GICE, with  
217 two further decreases occurring temporally close to the HICE<sup>3,54</sup>. Our approach considers  
218 many eruptions to estimate nutrient supply on a coarse scale. The super-eruptions represented  
219 by bentonites would likely have led to initial cooling (due to injection of stratospheric  
220 aerosols), followed by warming (from CO<sub>2</sub> injection), before cooling because of increases in  
221 nutrient supply and associated productivity levels. The warming/cooling cycles this scenario  
222 represents are purportedly dangerous for organisms, with biodiversity loss occurring when  
223 temperatures fall outside the optimal window<sup>3</sup>, potentially explaining the LOME initiation.  
224 Due to their global nature, we focus on the HICE and GICE, and only model two P pulses.  
225 However, bentonite ages suggest that multiple eruptions occurred between the two largest  
226 volcanic episodes and CIEs (Fig. 1), which may have led to transient local CIEs, such as those  
227 reported in the Scandinavian sections<sup>7</sup>.

228 In addition to releasing nutrients, it is possible that other toxic metals are also released  
229 during ash alteration and diagenesis<sup>25</sup>. During the Hirnantian glaciation and the HICE, there is  
230 evidence for metal-induced malformations in fossil plankton assemblages<sup>55</sup>. Further, volcanic  
231 ash may lead to the formation of large-scale anoxic conditions below deposited blankets<sup>24</sup>,  
232 which may have further enhanced redox-based recycling of toxic metals<sup>55</sup> and led to the  
233 deposition of widespread black shales<sup>47</sup>. Using the evidence presented here, we conclude that  
234 the pulsed nature of global cooling at this time appears to be a result of the eruption of two  
235 distinct volcanic provinces, one in what is now North America and the Baltic, and one in what  
236 is now Southern China. Further, our models suggest that the deposition of extensive ash  
237 blankets and weathering of lavas emplaced during Late Ordovician volcanism, supplied  
238 sufficient P to drive global cooling, glaciation, and the LOME.

### 239 **Acknowledgements**

240 This work was funded by NERC grant NE/K00543X/1, “The role of marine diagenesis of  
241 tephra in the carbon cycle”. B.J.W.M. acknowledges support from NERC grant  
242 NE/S009663/1. T.M.G. acknowledges support of NERC grant NE/R004978/1, and funding  
243 from the Alan

244 Turing Institute (EP/N510129/1). We are grateful for comments from Christian Rasmussen  
245 and the anonymous reviewer(s), which helped to improve the manuscript. We are grateful to  
246 staff of the IODP Gulf Coast Repository and IODP Kochi Core Repository for their assistance  
247 during sampling of cores U1396C and U1339D, respectively.

### 248 **Author Contributions**

249 J.L., T.M.G. and M.R.P. conceived this research. J.L. and H.R.M. completed the laboratory  
250 analyses. B.J.W.M. completing the modelling and J.L. compiled and analysed the data. J.L.

251 and B.J.W.M. created the figures. J.L. and B.J.W.M. wrote the manuscript, with input from  
252 T.M.G., H.R.M. and M.R.P.

### 253 **Competing Interests**

254 The authors declare no competing interests.

### 255 **Corresponding Author**

256 All correspondence and request for materials should be addressed to Jack Longman  
257 ([jack.longman@uni-oldenburg.de](mailto:jack.longman@uni-oldenburg.de))

### 258 **Figure Captions**

259 **Figure 1: Compilation of Late Ordovician bentonite ages from North America and**  
260 **China.** Bentonites ages in North America/Scandinavia (**a**), and China (**b**). Each age is  
261 represented by a probability density curve derived from published mean and standard  
262 deviation, from which 10,000 Monte Carlo simulations were completed and binned at 0.25  
263 Myr intervals to attain probability densities of the eruption occurring in each bin. Colours  
264 correspond to the studies from which each age is obtained. **c**, Average probability densities  
265 for each 0.25 Myr bin, for the North American (blue) and Chinese bentonites (red). Vertical  
266 lines indicate the bin in which bentonite deposition is most likely. (See Supplementary Tables  
267 4 and 5 for references).

268 **Figure 2: Paleogeographic reconstruction for the Late Ordovician at c. 450 Ma (Katian).**

269 Marked with ellipses are the two volcanic provinces investigated in this study, with blue  
270 ellipses representing the North American and Scandinavian province, and a green ellipse to  
271 represent the Chinese province. The base map was constructed using the plate tectonic  
272 reconstructions from ref.<sup>56</sup> and is based partly on ref<sup>57</sup>.

**Figure 3: Box and whisker diagrams of phosphorus depletion, an indicator of the amount of phosphorus lost to the ocean, from ten present-day representative volcanic provinces (a).** Boxes are defined between the

275 first and third quartile (the interquartile range, IQR), with minimum and maximum whiskers  
276 representative of 1.5 times the IQR. Also shown is a map of each volcanic province used for  
277 this reconstruction **(b)**, with the provinces identified by numbers given in panel **(a)**. **Figure 4:**  
278 **Monte Carlo simulations of phosphorus supply from volcanic weathering during the**  
279 **Late Ordovician, with variable distributions defined by our ash depletion and**  
280 **weathering model. (a) and (b) represent P supply from ash deposition and diagenesis. In both**  
281 **panels, the total ash volume is presented along the x-axis, with total phosphorus supply on the**  
282 **y-axis. Each Monte Carlo simulation is indicated by a circle, with the colour indicating the**  
283 **depletion factor. (c) Estimate of P flux resulting from weathering of terrestrial volcanic matter**  
284 **(y-axis), plotted against the area covered by this ash and lava. Again, each simulation is**  
285 **indicated by a filled circle, with the colour denoting the rate of phosphorus supply.**

286 **Figure 5. Biogeochemical model outputs for impacts of volcanism during the GICE and**  
287 **HICE. COPSE model baseline runs<sup>39</sup> plus P supply from ash. a, Grey lines show the P input**  
288 **Gaussian functions (see text). The P input magnitude follows the mean or 95<sup>th</sup> percentiles of**  
289 **the values derived for ash supply and weathering combined, with or without recycling of P**  
290 **from sediments (see main text). b, Modelled  $\delta^{13}\text{C}$  of carbonates (with colours defined in panel**  
291 **e) compared to data<sup>50</sup> (yellow circles). c, Modelled atmospheric  $\text{CO}_2$ . d, Modelled global**  
292 **average surface temperature. e, Degree of marine anoxia (represented as the modelled**  
293 **proportion of anoxic seafloor). Solid lines show the same simulations as the dashed lines, but**  
294 **with additional P input to represent sedimentary recycling of P (see text).**

## 295 **References**

- 296 1. Harper, D. A. T., Hammarlund, E. U. & Rasmussen, C. M. Ø. End Ordovician extinctions: A  
297 coincidence of causes. *Gondwana Res.* 25, 1294–1307 (2014).
- 298 2. Bambach, R. K., Knoll, A. H. & Wang, S. C. Origination, extinction, and mass depletions of  
299 marine diversity. *Paleobiology* 30, 522–542 (2004).

- 300 3. Rasmussen, C. M. Ø., Kröger, B., Nielsen, M. L. & Colmenar, J. Cascading trend of Early  
301 Paleozoic marine radiations paused by Late Ordovician extinctions. *Proc. Natl. Acad. Sci. U. S. A.*  
302 116, 7207–7213 (2019).
- 303 4. Bergström, S. M., Schmitz, B., Saltzman, M. R. & Huff, W. D. The Upper Ordovician  
304 Guttenberg  $\delta^{13}\text{C}$  excursion (GICE) in North America and Baltoscandia: Occurrence,  
305 chronostratigraphic significance, and paleoenvironmental relationships. *Geol. Soc. Am. Spec. Pap.*  
306 466, 37–67 (2010).
- 307 5. Metzger, J. G., Ramezani, J., Bowring, S. A. & Fike, D. A. New age constraints on the  
308 duration and origin of the Late Ordovician Guttenberg  $\delta^{13}\text{C}_{\text{carb}}$  excursion from high-precision U-Pb  
309 geochronology of K-bentonites. *GSA Bull.* (2020) doi:10.1130/B35688.1.
- 310 6. Finnegan, S. et al. The magnitude and duration of late Ordovician-early Silurian glaciation.  
311 *Science*. 331, 903–906 (2011).
- 312 7. Ainsaar, L. et al. Middle and Upper Ordovician carbon isotope chemostratigraphy in  
313 Baltoscandia: A correlation standard and clues to environmental history. *Palaeogeogr. Palaeoclimatol.*  
314 *Palaeoecol.* 294, 189–201 (2010).
- 315 8. Lenton, T. M., Crouch, M., Johnson, M., Pires, N. & Dolan, L. First plants cooled the  
316 Ordovician. *Nat. Geosci.* 5, 86–89 (2012).
- 317 9. Mills, B. J. W. et al. Modelling the long-term carbon cycle, atmospheric  $\text{CO}_2$ , and Earth  
318 surface temperature from late Neoproterozoic to present day. *Gondwana Research* vol. 67 172–186  
319 (2019).
- 320 10. Shen, J. et al. Improved efficiency of the biological pump as a trigger for the Late Ordovician  
321 glaciation. *Nat. Geosci.* 11, 510–514 (2018).
- 322 11. Swanson-Hysell, N. L. & Macdonald, F. A. Tropical weathering of the Taconic orogeny as a  
323 driver for Ordovician cooling. *Geology* 45, 719–722 (2017).

- 324 12. Bartlett, R. et al. Abrupt global-ocean anoxia during the Late Ordovician–early Silurian  
325 detected using uranium isotopes of marine carbonates. *Proc. Natl. Acad. Sci. U. S. A.* 115, 5896–5901  
326 (2018).
- 327 13. Morris, J. L. et al. The timescale of early land plant evolution. *Proc. Natl. Acad. Sci. U. S. A.*  
328 115, E2274–E2283 (2018).
- 329 14. Buggisch, W. et al. Did intense volcanism trigger the first Late Ordovician icehouse? *Geology*  
330 38, 327–330 (2010).
- 331 15. Herrmann, A. D., Leslie, S. A. & MacLeod, K. G. Did intense volcanism trigger the first Late  
332 Ordovician icehouse?: COMMENT. *Geology* 39, e237–e237 (2011).
- 333 16. Huff, W. D., Bergström, S. M. & Kolata, D. R. Ordovician explosive volcanism. *Geol. Soc.*  
334 *Am. Spec. Pap.* 466, 13–28 (2010).
- 335 17. Tao, H., Qiu, Z., Lu, B., Liu, Y. & Qiu, J. Volcanic activities triggered the first global cooling  
336 event in the Phanerozoic. *J. Asian Earth Sci.* 104074 (2019) doi:10.1016/j.jseas.2019.104074.
- 337 18. Huff, W. D., Kolata, D. R., Bergström, S. M. & Zhang, Y. S. Large-magnitude Middle  
338 Ordovician volcanic ash falls in North America and Europe: Dimensions, emplacement and post-  
339 emplacement characteristics. *J. Volcanol. Geotherm. Res.* 73, 285–301 (1996).
- 340 19. Sell, B. K. et al. Stratigraphic correlations using trace elements in apatite from late Ordovician  
341 (Sandbian-Katian) K-bentonites of eastern North America. *Bull. Geol. Soc. Am.* 127, 1259–1274  
342 (2015).
- 343 20. Ballo, E. G., Augland, L. E., Hammer, Ø. & Svensen, H. H. A new age model for the  
344 Ordovician (Sandbian) K-bentonites in Oslo, Norway. *Palaeogeogr. Palaeoclimatol. Palaeoecol.* 520,  
345 203–213 (2019).
- 346 21. Liu, W. et al. K-bentonites in Ordovician-Silurian transition from South China: Implications  
347 for tectonic evolution in the northern margin of Gondwana. *J. Geol. Soc. London.* jgs2020-049 (2020)  
348 doi:10.1144/jgs2020-049.

- 349 22. Smolarek-Lach, J., Marynowski, L., Trela, W. & Wignall, P. B. Mercury Spikes Indicate a  
350 Volcanic Trigger for the Late Ordovician Mass Extinction Event: An Example from a Deep Shelf of  
351 the Peri-Baltic Region. *Sci. Rep.* 9, 1–11 (2019).
- 352 23. Jones, D. S., Martini, A. M., Fike, D. A. & Kaiho, K. A volcanic trigger for the late  
353 Ordovician mass extinction? Mercury data from south China and Laurentia. *Geology* 45, 631–634  
354 (2017).
- 355 24. Longman, J., Palmer, M. R., Gernon, T. M. & Manners, H. R. The role of tephra in enhancing  
356 organic carbon preservation in marine sediments. *Earth-Science Rev.* 192, 480–490 (2019).
- 357 25. Jones, M. T. & Gislason, S. R. Rapid releases of metal salts and nutrients following the  
358 deposition of volcanic ash into aqueous environments. *Geochim. Cosmochim. Acta* 72, 3661–3680  
359 (2008).
- 360 26. Sell, B., Ainsaar, L. & Leslie, S. Precise timing of the Late Ordovician (Sandbian) super-  
361 eruptions and associated environmental, biological, and climatological events. *J. Geol. Soc. London.*  
362 170, 711–714 (2013).
- 363 27. Tucker, R. D. & McKerrow, W. S. Early Paleozoic chronology: a review in light of new U-Pb  
364 zircon ages from Newfoundland and Britain. *Can. J. Earth Sci.* 32, 368–379 (1995).
- 365 28. Ling, M. X. et al. An extremely brief end Ordovician mass extinction linked to abrupt onset of  
366 glaciation. *Solid Earth Sci.* 4, 190–198 (2019).
- 367 29. Du, X. et al. Was volcanic activity during the Ordovician-Silurian transition in South China  
368 part of a global phenomenon? Constraints from zircon U–Pb dating of volcanic ash beds in black  
369 shales. *Mar. Pet. Geol.* 114, 104209 (2020).
- 370 30. Lee, C.-T. A. et al. Volcanic ash as a driver of enhanced organic carbon burial in the  
371 Cretaceous. *Sci. Rep.* 8, 4197 (2018).
- 372 31. Longman, J., Palmer, M. R., Gernon, T. M. & Manners, H. R. Subaerial volcanism is a major  
373 contributor to oceanic iron and manganese cycles. In Review.

- 374 32. Gudmundsson, M. T. et al. Ash generation and distribution from the April-May 2010 eruption  
375 of Eyjafjallajökull, Iceland. *Sci. Rep.* 2, 572 (2012).
- 376 33. Laeger, K. et al. High-resolution geochemistry of volcanic ash highlights complex magma  
377 dynamics during the Eyjafjallajökull 2010 eruption. *Am. Mineral.* 102, 1173–1186 (2017).
- 378 34. Paytan, A. & McLaughlin, K. The oceanic phosphorus cycle. *Chem. Rev.* 107, 563–576  
379 (2007).
- 380 35. Cao, W., Lee, C. T. A. & Lackey, J. S. Episodic nature of continental arc activity since 750  
381 Ma: A global compilation. *Earth Planet. Sci. Lett.* 461, 85–95 (2017).
- 382 36. Mills, B. J. W., Scotese, C. R., Walding, N. G., Shields, G. A. & Lenton, T. M. Elevated CO<sub>2</sub>  
383 degassing rates prevented the return of Snowball Earth during the Phanerozoic. *Nat. Commun.* 8, 1–7  
384 (2017).
- 385 37. Dessert, C., Dupré, B., Gaillardet, J., François, L. M. & Allègre, C. J. Basalt weathering laws  
386 and the impact of basalt weathering on the global carbon cycle. *Chem. Geol.* 202, 257–273 (2003).
- 387 38. Dessert, C. et al. Erosion of Deccan Traps determined by river geochemistry: impact on the  
388 global climate and the <sup>87</sup>Sr/<sup>86</sup>Sr ratio of seawater. *Earth Planet. Sci. Lett.* 188, 459–474 (2001).
- 389 39. Tostevin, R. & Mills, B. J. W. Reconciling proxy records and models of Earth’s oxygenation  
390 during the Neoproterozoic and Palaeozoic. *Interface Focus* 10, 20190137 (2020).
- 391 40. Slomp, C. P. & Van Cappellen, P. The global marine phosphorus cycle: sensitivity to oceanic  
392 circulation. *Biogeosciences* 4, 155–171 (2007).
- 393 41. Hallam, A. *Phanerozoic sea-level changes.* (Columbia Univeristy Press, 1992).
- 394 42. Walker, L. J., Wilkinson, B. H. & Ivany, L. C. Continental drift and phanerozoic carbonate  
395 accumulation in shallow-shelf and deep-marine settings. *J. Geol.* 110, 75–87 (2002).
- 396 43. Alcott, L. J., Mills, B. J. W. & Poulton, S. W. Stepwise Earth oxygenation is an inherent  
397 property of global biogeochemical cycling. *Science.* 366, 1333–1337 (2019).



- 398 44. Berner, R. A. A model for atmospheric CO<sub>2</sub> over Phanerozoic time. *Am. J. Sci.* 291, 339–376  
399 (1991).
- 400 45. Witkowski, C. R., Weijers, J. W. H., Blais, B., Schouten, S. & Sinninghe Damsté, J. S.  
401 Molecular fossils from phytoplankton reveal secular PCO<sub>2</sub> trend over the phanerozoic. *Sci. Adv.* 4,  
402 eaat4556 (2018).
- 403 46. Goldberg, S. L., Present, T. M., Finnegan, S. & Bergmann, K. D. A high-resolution record of  
404 early Paleozoic climate. *Proc. Natl. Acad. Sci.* 118, (2021).
- 405 47. Zou, C. et al. Organic-matter-rich shales of China. *Earth-Science Reviews* vol. 189 51–78  
406 (2019).
- 407 48. Su, W. et al. K-bentonite, black-shale and flysch successions at the Ordovician-Silurian  
408 transition, South China: Possible sedimentary responses to the accretion of Cathaysia to the Yangtze  
409 Block and its implications for the evolution of Gondwana. *Gondwana Res.* 15, 111–130 (2009).
- 410 49. LaPorte, D. F. et al. Local and global perspectives on carbon and nitrogen cycling during the  
411 Hirnantian glaciation. *Palaeogeogr. Palaeoclimatol. Palaeoecol.* 276, 182–195 (2009).
- 412 50. Saltzman, M. R. & Thomas, E. Carbon isotope stratigraphy. in *The Geologic Time Scale 2012*  
413 (eds. Gradstein, F. M., Ogg, J., Schmitz, M. D. & Ogg, G, M.) 207–232 (Elsevier, 2012).  
414 doi:10.1016/B978-0-444-59425-9.00011-1.
- 415 51. Sobolev, S. V. et al. Linking mantle plumes, large igneous provinces and environmental  
416 catastrophes. *Nature* 477, 312–316 (2011).
- 417 52. Black, B. A. et al. Systemic swings in end-Permian climate from Siberian Traps carbon and  
418 sulfur outgassing. *Nat. Geosci.* 11, 949–954 (2018).
- 419 53. Schoene, B., Guex, J., Bartolini, A., Schaltegger, U. & Blackburn, T. J. Correlating the end-  
420 Triassic mass extinction and flood basalt volcanism at the 100 ka level. *Geology* 38, 387–390 (2010).
- 421 54. Fan, J. X. et al. A high-resolution summary of Cambrian to early Triassic marine invertebrate  
422 biodiversity. *Science* . 367, 272–277 (2020).

423 55. Vandenbroucke, T. R. A. et al. Metal-induced malformations in early Palaeozoic plankton are  
424 harbingers of mass extinction. *Nat. Commun.* 6, (2015).

425 56. Merdith, A. S. et al. Extending full-plate tectonic models into deep time: Linking the  
426 Neoproterozoic and the Phanerozoic. *Earth-Science Rev.* 214, 103477 (2021).

427 57. Cocks, L. R. M. & Torsvik, T. H. Ordovician palaeogeography and climate change.  
428 *Gondwana Res.* (2020) doi:10.1016/j.gr.2020.09.008.

429

## 430 **Methods**

### 431 **Major and trace element geochemistry**

432 Tephra layers from IODP cores 1396C (Lesser Antilles) and U1339D (Bering Sea)  
433 were analysed for their phosphorus content. Tephtras were identified visually, and  
434 microscopically, in core 1339D and through their low CaCO<sub>3</sub> content in U1396C. P was  
435 analysed in tephra layers after mixed acid (HNO<sub>3</sub>-HCl-HF) bench-top digestion. Samples  
436 were then analysed on a Perkin Elmer 2000B at the University of Oxford. Analysis was  
437 completed in both standard mode (m/z 31) and in reaction mode, with O<sub>2</sub> as reaction gas and  
438 analysis on m/z 47. In all cases, data were more accurate and detection limits were sufficient  
439 from standard mode analysis and so we present these results here. Blanks and standards  
440 (BHVO2 basalt) were prepared and analysed in the same manner (Supplementary Table 1).  
441 For cores U1396C and U1339D, Al and Zr were determined after digestion using the same  
442 procedure as above, again alongside standard BHVO2 and blanks. Concentrations of these  
443 elements were determined using a Thermo X-Series ICP-MS at the University of  
444 Southampton (Supplementary Table 1).

### 445 **P depletion factors and P release**

446 We used the GEOROC database to estimate the protolith composition of volcanic  
447 material from each of the source regions. These data were filtered to remove any data related

448 to non-outcrop samples, xenoliths and any mineral-specific analyses. This database was used  
 449 to estimate the composition of tephra prior to dissolution and diagenetic alteration. By  
 450 normalising P to Zr and plotting this ratio against Ti/Zr (elements which are largely immobile  
 451 during diagenesis), the empirical relationship between the two ratios can be used to estimate  
 452 the original protolith composition following the method of ref.<sup>30</sup>, developed to estimate metal  
 453 mobility in Cretaceous tephra (Supplementary Table 2). The linear regression representing  
 454 this relationship is then used back-calculate the original composition of altered tephra  
 455 (Supplementary Tables 2, 3, refs.<sup>58-64</sup>). These compositions, along with compositions of  
 456 altered tephra, are then used to calculate depletion factors using the following equation  
 457 (Equation 1):

$$P_D = \frac{M_P^L}{M_P^O} = 1 - \frac{\left(\frac{C_P^{re}}{C_{Zr}^{re}}\right)}{\left(\frac{C_P^O}{C_{Zr}^O}\right)} \text{ (Eq. 1)}$$

458 The left side of the equation is the depletion factor, where  $M_P^O$  original P mass in the protolith,  
 459  $M_P^L$  is the loss of P.  $C_P^{re}$  and  $C_{Zr}^{re}$  are the mass of P and Zr in tephra, and  $C_P^O/C_{Zr}^O$  represents the  
 460 ratio of P to Zr in the protolith, back-calculated from the linear regression of GEOROC data  
 461 (Fig. 3, Extended Data Figures 1, 2).

## 462 **Estimating the extent and timing of volcanism during the Late Ordovician**

463 We use Monte Carlo simulations of variables associated with bentonite deposition  
 464 during the Late Ordovician to estimate the size of the volcanic eruptions and associated ash  
 465 deposition<sup>57</sup>. For the GICE period, we use values from published compilations of North  
 466 American bentonites<sup>5,19</sup> (Supplementary Table 4), and for the HICE we collate ages from  
 467 published bentonites from China (Supplementary Table 5). For the period 455 – 450 Ma  
 468 (corresponding to period covering the GICE), we take the number of ash layers to be 100  
 469 based on observations<sup>19</sup>. We assume these ash layers represent eruptions of VEI 8 due to the

470 location and characteristics of these bentonites, which constitute discrete centimetre-thick  
471 horizons thousands of kilometres from any proposed source<sup>16,19</sup>. We assume each eruption  
472 contained on average 1000 km<sup>3</sup> erupted material<sup>18</sup>. To estimate how much erupted material  
473 was ash, we use a value of 50%, representing the likely proportions in Ultraplinian  
474 eruptions<sup>18,21</sup>. Since we are only interested, in the first instance, in the ash which may directly  
475 supply P to the ocean, we use an estimate of 50% ashfall in the ocean basins. This number is  
476 based upon estimates of ashfall which has been subducted since the Ordovician, using  
477 isopachs constructed from North American outcrops<sup>18</sup>, and paleogeographic reconstructions  
478 which indicate volcanism was linked to the opening of the Iapetus Ocean (Figure 2). For all  
479 variables used in equation 2, we apply standard deviations of all variables set at 25% of the  
480 variable mean, unless stated (Supplementary Table 6). 10,000 simulations of all variables  
481 were performed using the R package *rtrucnorm*, and outputs were used to reconstruct likely  
482 ash volumes (in km<sup>3</sup>).

483 For the period 450 – 440 Ma (corresponding to period covering the HICE), a similar  
484 set of likely values for variables was constructed using published data on Chinese bentonite  
485 deposits<sup>21</sup>. In this case, we use 88 ash layers as our mean, derived from the subtraction of 16  
486 Silurian ashes from a compilation of Late Ordovician–early Silurian Chinese bentonites<sup>21,65</sup>.  
487 We use 75% as the oceanic fraction because this volcanism was linked with subduction of the  
488 Zhenge-Dapu Ocean (Figure 2), and so a high proportion will be deposited in this  
489 environment<sup>21</sup>. Again, we apply standard deviations of 25% to each of these variables to  
490 consider the uncertainty.

491 In both cases, to estimate ash density, and the amount of P contained in the original  
492 ashes, we use measured values from Icelandic ashfall<sup>32,33</sup>, with standard deviations derived  
493 from the measurements. Using the ash volume estimates derived from these variables, and our

494 depletion factors, we simulate 10,000 iterations for total P supply for each period (in mole P),  
495 using the following equation (Eq. 2):

496 
$$P \text{ release (mole)} = \left( \frac{V_{\text{Ash}} \times \rho_{\text{Ash}} \times P_{\text{Ash}} \times P_D}{30.97} \right) \times P_{\text{ocean}} \text{ (Equation 2)}$$

497 where  $V_{\text{Ash}}$ ,  $\rho_{\text{Ash}}$  and  $P_{\text{Ash}}$  are the volume of ash (in  $\text{km}^3$ ), density of ash (in  $\text{kg}/\text{m}^3$ ) and  
498 phosphorus content in ash (in wt %).  $P_D$  is the depletion factor of phosphorus,  $P_{\text{ocean}}$  is the  
499 proportion falling into the ocean and 30.97 is the molecular weight of P, to convert from  
500 grams to moles. Such an exercise provides an absolute amount of P released for each period,  
501 but for modelling purposes, we must convert our total P supply values into flux (in  $\text{mol P myr}^{-1}$ ).  
502 <sup>1</sup>).

503 To do this, we develop a dataset of all reliably dated (i.e., excluding K-Ar or fission  
504 track dates) bentonites of Late Ordovician age from across the two primary volcanic  
505 provinces, China and North America/Baltica (Figure 2, refs. <sup>5,20,21,26–29,65–80</sup>). For each of the  
506 dates, we use a Monte Carlo based approach to generate 10,000 possible ages, constrained by  
507 published age and error values. We group the outputs of this exercise into 0.25 Myr bins and  
508 produce probability density estimates for each bin (Fig. 1a, b). For each of the two volcanic  
509 provinces, we average across each bin to result in a probability density of each 0.25 Myr  
510 period (Fig. 1c). This exercise results in two distinct peaks, representing the most likely  
511 period of volcanism for both provinces. For North America/Scandinavia, this peak is centred  
512 on 453.5 Ma. For China, the volcanic peak occurs 444.0 Ma. To represent these events in the  
513 model we then use a standard Gaussian curve with  $\sigma=0.4$ , giving an event duration of around  
514 2 Myrs. This width is informed by the duration of the carbon isotope excursions.

### 515 **Estimating P flux from weathering**

516 We estimate the spatial extent of erupted material during the Late Ordovician using an  
517 averaged value from a modelling study of Ordovician volcanism ( $1.56 \times 10^6 \text{ km}^2$ ; ref.<sup>60</sup>). We

518 then use P release value of 29.77 kg P km<sup>-2</sup> yr<sup>-1</sup> as measured from basalts<sup>82</sup>. We estimate that  
519 50% of the ash and lava was terrestrially emplaced based on the observations of ash  
520 deposition considered previously<sup>18,21</sup>. By applying 20% errors to all of these values, we then  
521 carried out 10,000 Monte Carlo simulations of each variable, before calculating the final flux  
522 (in mol P myr<sup>-1</sup>) by multiplying each iteration of each variable.

### 523 **Biogeochemical modelling**

524 We use the latest COPSE biogeochemical model<sup>39</sup>. We run the model baseline and add  
525  $P_{force}$  to the global bioavailable phosphorus weathering flux (Equation 3). This adds additional  
526 phosphorus input during the Late Ordovician to the baseline model run.

$$527 P_{force} = 10^{-6} P_{GICE} \frac{norm(t, -453.45, 0.4)}{norm(-453.45, -453.45, 0.4)} + 10^{-6} P_{HICE} \frac{norm(t, -444, 0.4)}{norm(-444, -444, 0.4)} \text{ (Eq. 3)}$$

528 Here  $P_{GICE}$  and  $P_{HICE}$  are the total P inputs from ash, weathering, and recycling in moles. Here  
529  $norm$  is a normal function defined as  $norm(time, midpoint, \sigma)$ .  $P_{force}$  is multiplied by 5 in some  
530 simulations to represent the additional recycling of P which is not captured in the COPSE  
531 model. This factor is determined by running a P-C cycling model which has an explicit  
532 representation of the shelf<sup>43</sup> and comparing the ratio between P input from weathering and  
533 overall marine P concentration versus the same metric in COPSE. The reader is referred to  
534 Extended Data Figure 3 for the model comparison plots.

### 535 **Data Availability**

536 The authors declare that data supporting the findings of this study are available within the  
537 article and Supplementary Information and Extended Data. All data have also been uploaded  
538 to Figshare, at the following DOI addresses: <http://dx.doi.org/10.6084/m9.figshare.14914893>,  
539 <http://dx.doi.org/10.6084/m9.figshare.14914911>,  
540 <http://dx.doi.org/10.6084/m9.figshare.14914896> and  
541 <http://dx.doi.org/10.6084/m9.figshare.14914890>.

542 **Code availability**

543 COPSE model code can be downloaded at <https://github.com/bjwmills>

544 **Methods-only References**

545 58. Bitschene, P. R., Mehl, K. W. & Schmincke, H.-U. Composition and origin of marine ash  
546 layers and epiclastic rocks from the Kerguelen Plateau, southern Indian Ocean (Legs 119 and 120).  
547 Proc. Ocean Drill. Program, 120 Sci. Results 120, 135–149 (1992).

548 59. Schindlbeck, J. C. et al. One Million Years tephra record at IODP Sites U1436 and U1437:  
549 Insights into explosive volcanism from the Japan and Izu arcs. *Isl. Arc* 27, e12244 (2018).

550 60. Rodehorst, U., Schmincke, H.-U. & Sumita, M. Geochemistry and petrology of Pleistocene  
551 ash layers erupted at Las Cañadas Edifice (Tenerife). *Scientific Results* vol. 157 (1998).

552 61. Salisbury, M. J. et al. Deep-sea ash layers reveal evidence for large, late Pleistocene and  
553 Holocene explosive activity from Sumatra, Indonesia. *J. Volcanol. Geotherm. Res.* 231–232, 61–71  
554 (2012).

555 62. Derkachev, A. N. et al. Tephra layers of in the quaternary deposits of the Sea of Okhotsk:  
556 Distribution, composition, age and volcanic sources. *Quat. Int.* 425, 248–272 (2016).

557 63. Schindlbeck, J. C. et al. Late Cenozoic tephrostratigraphy offshore the southern Central  
558 American Volcanic Arc: 1. Tephra ages and provenance. *Geochemistry, Geophys. Geosystems* 17,  
559 4641–4668 (2016).

560 64. Allan, A. S. R., Baker, J. A., Carter, L. & Wysoczanski, R. J. Reconstructing the Quaternary  
561 evolution of the world's most active silicic volcanic system: insights from an ~1.65 Ma deep ocean  
562 tephra record sourced from Taupo Volcanic Zone, New Zealand. *Quat. Sci. Rev.* 27, 2341–2360  
563 (2008).

564 65. Yang, S. et al. Duration, evolution, and implications of volcanic activity across the  
565 Ordovician–Silurian transition in the Lower Yangtze region, South China. *Earth Planet. Sci. Lett.* 518,  
566 13–25 (2019).

- 567 66. Tucker, R. D. U-Pb dating of Plinian-eruption ashfalls by the isotopic dilution method: a  
568 reliable and precise tool for time-scale calibration and biostratigraphic correlation. *Geol. Soc. Amer.*  
569 *Abs. w/ Prog.* 24, A192 (1992).
- 570 67. Oruche, N. E., Dix, G. R. & Kamo, S. L. Lithostratigraphy of the upper Turinian – Lower  
571 Chatfieldian (upper Ordovician) foreland succession, and a U–Pb ID–TIMS date for the Millbrig  
572 volcanic ash bed in the Ottawa embayment. *Can. J. Earth Sci.* 55, 1079–1102 (2018).
- 573 68. Min, K., Renne, P. R. & Huff, W. D. Ar/Ar dating of Ordovician K-bentonites in Laurentia  
574 and Baltoscandia. *Earth Planet. Sci. Lett.* 185, 121–134 (2001).
- 575 69. Samson, S. D., Patchett, P. J., Roddick, J. C. & Parrish, R. R. Origin and tectonic setting of  
576 Ordovician bentonites in North America: isotopic and age constraints. *Geol. Soc. Am. Bull.* 101,  
577 1175–1181 (1989).
- 578 70. Svensen, H. H., Hammer, Ø. & Corfu, F. Astronomically forced cyclicity in the Upper  
579 Ordovician and U-Pb ages of interlayered tephra, Oslo Region, Norway. *Palaeogeogr. Palaeoclimatol.*  
580 *Palaeoecol.* 418, 150–159 (2015).
- 581 71. Bauert, H. et al. New U-Pb zircon ages of the Sandbian (Upper Ordovician) ‘Big K-bentonite’  
582 in Baltoscandia (Estonia and Sweden) by LA-ICPMS. *GFF* 136, 30–33 (2014).
- 583 72. Compston, W. & Williams, I. S. Ion probe ages for the British Ordovician and Silurian  
584 stratotypes. in *Global perspectives on Ordovician geology* (eds. Webby, B. D. & Laurie, J. R.) 59–67  
585 (1992).
- 586 73. Li, Y., Zhang, T., Shao, D. & Shen, B. New U-Pb zircon age and carbon isotope records from  
587 the Lower Silurian Longmaxi Formation on the Yangtze Platform, South China: Implications for  
588 stratigraphic correlation and environmental change. *Chem. Geol.* 509, 249–260 (2019).
- 589 74. Hu, Y. H., Zhou, J. Bin, Song, B., Li, W. & Sun, W. D. SHRIMP zircon U-Pb dating from K-  
590 bentonite in the top of Ordovician of Wangjiawan section, Yichang, Hubei, China. *Sci. China, Ser. D*  
591 *Earth Sci.* 51, 493–498 (2008).



- 592 75. Xie, S., Wang, Z., Wang, J. & Zhuo, J. LA-ICP-MS zircon U-Pb dating of the bentonites from  
593 the uppermost part of the Ordovician Wufeng Formation in the Haoping section, Taoyuan, Hunan.  
594 *Sediment. Tethyan Geol.* 4, 597 (2012).
- 595 76. Yang, S. et al. Constraints on the accumulation of organic matter in Upper Ordovician-lower  
596 Silurian black shales from the Lower Yangtze region, South China. *Mar. Pet. Geol.* 120, 104544  
597 (2020).
- 598 77. Ge, X. et al. Mineralogical and geochemical characteristics of K-bentonites from the Late  
599 Ordovician to the Early Silurian in South China and their geological significance. *Geol. J.* 54, 514–528  
600 (2019).
- 601 78. Zheng, B. et al. Nature of the Late Ordovician-Early Silurian Xiaohe section, Hunan-Hubei  
602 area, South China: implications for the Kwangsi Orogeny. *Int. Geol. Rev.* 62, 1262–1272 (2020).
- 603 79. Kunk, M. J., Sutter, J., Obradovich, J. D. & Lanphere, M. A. Age of biostratigraphic horizons  
604 within the Ordovician and Silurian systems. *Geol. Soc. Mem.* 10, 89–92 (1985).
- 605 80. Tucker, R. D., Krogh, T. E., Ross, R. J. & Williams, S. H. Time-scale calibration by high-  
606 precision UPb zircon dating of interstratified volcanic ashes in the Ordovician and Lower Silurian  
607 stratotypes of Britain. *Earth Planet. Sci. Lett.* 100, 51–58 (1990).
- 608 81. Lefebvre, V., Servais, T., François, L. & Averbuch, O. Did a Katian large igneous province  
609 trigger the Late Ordovician glaciation?. A hypothesis tested with a carbon cycle model. *Palaeogeogr.*  
610 *Palaeoclimatol. Palaeoecol.* 296, 310–319 (2010).
- 611 82. Hartmann, J., Moosdorf, N., Lauerwald, R., Hinderer, M. & West, A. J. Global chemical  
612 weathering and associated p-release - the role of lithology, temperature and soil properties. *Chem.*  
613 *Geol.* 363, 145–163 (2014).

1 **Late Ordovician climate change and extinctions driven by elevated volcanic nutrient**  
2 **supply**

3  
4 Jack Longman<sup>1,2,\*</sup>, Benjamin J. W. Mills<sup>3</sup>, Hayley R. Manners<sup>4,5</sup>, Thomas M. Gernon<sup>4</sup> and  
5 Martin R. Palmer<sup>4</sup>

6 <sup>1</sup> Marine Isotope Geochemistry, Institute for Chemistry and Biology of the Marine  
7 Environment (ICBM), University of Oldenburg, PO Box 2503, 26111 Oldenburg, Germany.

8 <sup>2</sup> School of Geography and the Environment, University of Oxford, South Parks Road,  
9 Oxford, OX1 3QY, UK.

10 <sup>3</sup> School of Earth and Environment, University of Leeds, Leeds LS2 9JT, UK.

11 <sup>4</sup> School of Ocean and Earth Sciences, University of Southampton, Southampton, SO14 3ZH,  
12 UK.

13 <sup>5</sup> School of Geography, Earth and Environmental Sciences, University of Plymouth,  
14 Plymouth, PL4 8AA, UK.

15  
16 \*Corresponding Author: [jack.longman@uni-oldenburg.de](mailto:jack.longman@uni-oldenburg.de)

17  
18 **Abstract**

19 **The Late Ordovician (~459–444 million years ago) was characterised by global cooling,**  
20 **glaciation and severe mass extinction. These events may have been driven by increased**  
21 **delivery of the nutrient phosphorus (P) to the ocean, and associated increases in marine**  
22 **productivity, but it is not clear why this occurred in the two pulses identified in the**  
23 **geological record. We link both cooling phases, and the extinction, to volcanic eruptions**  
24 **through marine deposition of nutrient-rich ash and the weathering of terrestrially**  
25 **emplaced ash and lava. We then reconstruct the influence of Late Ordovician volcanic P**  
26 **delivery on the marine system by coupling an estimate of bioavailable phosphate supply**

27 (derived from a depletion and weathering model) to a global biogeochemical model. Our  
28 model compares volcanic ash P content in marine sediments before and after alteration  
29 to determine depletion factors, and we find good agreement with observed carbon  
30 isotope and reconstructed temperature shifts. Hence, massive volcanism can drive  
31 substantial global cooling on million-year timescales due to P delivery associated with  
32 long-term weathering of volcanic deposits, offsetting the transient warming of  
33 greenhouse gas emission associated with volcanic eruptions. Such longer-term cooling  
34 and potential for marine eutrophication may be important for other volcanism-driven  
35 global events.

### 36 Main Text

37 The Late Ordovician mass extinction (LOME) occurred in two phases, and in terms of species  
38 loss was the second greatest extinction event in Earth's history<sup>1-3</sup>. The Late Ordovician is  
39 characterised by a number of carbon isotope excursions (CIEs), with two globally-  
40 represented, the Guttenburg (GICE) at ~454 Ma, and Hirnantian (HICE) at ~ 445 Ma<sup>4</sup>. The  
41 GICE coincides with global cooling, and the beginning of the HICE is associated with  
42 widespread glaciation, with the cooling periods generally implicated in instigating the  
43 LOME<sup>1,5-7</sup>.

44 The primary driver behind the CIEs and associated cooling is uncertain. One  
45 possibility is that the emergence of early nonvascular land plants amplified terrestrial  
46 weathering and increased the delivery of the key limiting nutrient phosphorus to the oceans<sup>8</sup>.  
47 Greater availability of phosphorus increases marine productivity and organic carbon burial,  
48 driving a reduction in atmospheric CO<sub>2</sub> and a positive excursion in carbonate  $\delta^{13}\text{C}$  (ref.<sup>9</sup>).  
49 Other proposals include an increasing fraction of eukaryotic marine production strengthening  
50 the biological pump<sup>10</sup>, and increased tropical weathering resulting from orogenesis  
51 augmenting the supply of phosphorus to the oceans<sup>11</sup>.

52           The concept that Late Ordovician cooling was driven by organic carbon burial is  
53 supported by observations<sup>12</sup>, but why this occurred in two distinct pulses during the GICE and  
54 HICE is unclear. This pulsing may have arisen from early plants colonising new terranes<sup>8</sup>, but  
55 there is little evidence for this, although poor fossil preservation cannot be ruled out<sup>13</sup>.  
56 Further, the pace of early plant evolution remains highly uncertain<sup>13</sup> and there is no evidence  
57 that eukaryotic evolution, or tropical uplift, occurred in distinct pulses. Existing global  
58 biogeochemical models cannot reliably reproduce the Hirnantian glaciation (or isotope  
59 excursions) associated with the HICE when based on known long-term tectonic cycles of  
60 uplift and degassing, and the positioning of the continents<sup>9</sup>, even though these models can  
61 accurately reproduce the Permo-Carboniferous and late Cenozoic icehouses<sup>9</sup>. This suggests  
62 that the Hirnantian icehouse was driven by some climatic forcing mechanism currently not  
63 well-represented in these models.

64           Given the potential association between volcanism and global climate change<sup>14,15</sup>, we  
65 explore the concept that Late Ordovician marine productivity and cooling episodes were  
66 directly related to subaerial volcanic activity. The Late Ordovician was characterised by  
67 extensive volcanic eruptions, preserved in the sedimentary record as bentonites<sup>16,17</sup>. These  
68 bentonites represent some of the largest volcanic eruptions in Earth's history, with estimates  
69 indicating some of the better studied events (Millbrig, Deicke and Kinnekulle) erupted  $\geq 1000$   
70 km<sup>3</sup> of pyroclastic material<sup>18</sup>. In addition, there are hundreds of spatially extensive bentonites  
71 of Late Ordovician (459 – 444 Ma) age preserved across North America<sup>19</sup>, Northern Europe<sup>20</sup>,  
72 and China<sup>16,21</sup>, prompting suggestions of a causal link between volcanism and global cooling  
73 during this period<sup>3,14,17</sup>. Most recently, several studies have employed the total organic carbon  
74 to mercury ratio (TOC/Hg), to directly link volcanic Hg emission to Late Ordovician climatic  
75 change (e.g. refs.<sup>22,23</sup>). However, it remains uncertain whether cooling was driven by rapid  
76 sulfate emissions, through the immediate weathering of ash and lava, or by longer-term

77 weathering of volcanic arcs and uplifted terranes<sup>17,23</sup>, a problem compounded by poorly  
78 constrained volcanic fluxes.

79 Volcanism may cool the climate on non-transitory timescales due to enhanced  
80 productivity and organic carbon preservation<sup>24</sup>, with one of the key drivers being enhanced P  
81 supply derived from leaching of volcanic ash<sup>25</sup>. It is not currently clear how much P may have  
82 been supplied from ash during the Late Ordovician, or how input of volcanic P may have  
83 influenced the marine environment. To answer these questions, we compile global data on P  
84 depletion in tephra layers today, as a method of quantifying P release to the ocean during ash  
85 deposition and diagenesis. We couple our estimates of P flux to a global biogeochemical  
86 model to investigate the potential impact of such nutrient supply to the Late Ordovician  
87 marine carbon cycle.

#### 88 **Timing and extent of volcanism during the Late Ordovician**

89 To estimate timing of volcanic activity, we compile 43 Ar-Ar and U-Pb dates from  
90 North American and Scandinavian bentonites (Fig. 1a), and 24 dates from Chinese bentonites  
91 of Late Ordovician age (Fig. 1b). Our reconstruction indicates that bentonite deposition  
92 occurred in two discrete pulses (Fig. 1c), corresponding to the eruption of two geographically  
93 distinct volcanic provinces (Figure 2). The first pulse represents North  
94 American/Scandinavian volcanism and is well-constrained, with the greatest depositional  
95 intensity occurring between 454.5 – 453 Ma, peaking at 453.5 Ma (Fig. 1c). This peak  
96 primarily represents highly-precise measurements of the North American “big” bentonites,  
97 the Deicke and Millbrig<sup>5,26</sup>, and the Grimstorp bentonite<sup>26</sup>. A slightly earlier peak is also  
98 apparent (c. 456.5 Ma), representing potentially uncertain estimates of the Kinnekulle  
99 bentonite age<sup>27</sup>, and other unnamed bentonites from Oslo<sup>20</sup> (see Supplementary Table 4).  
100 Chinese bentonite ages exhibit more spread, with fewer highly precise dates (Fig. 1c). Our  
101 compilation suggests the most intense volcanism in the China region occurred between 445.25

102 – 442.5 Ma, with a peak at about 444 Ma (Fig. 1c), corresponding to some of the most  
103 accurate dates from outcrop in the south-western Yunnan province<sup>28</sup>, and central Hubei  
104 province<sup>29</sup>. These two volcanic pulses correspond well to the two primary carbon isotope  
105 excursions of the Late Ordovician, the GICE and HICE, and may thus support a link between  
106 volcanism and climate change.

### 107 **P release during ash deposition, diagenesis and weathering**

108 To investigate this hypothesis, we estimate the amount of P which may have been  
109 supplied by the two main pulses of volcanism. To estimate the percentage of P released  
110 during ash deposition and diagenesis, altered ash compositions are compared to unaltered  
111 protolith compositions to estimate metal mobility<sup>30,31</sup>, using protolith data from the GEOROC  
112 database (<http://georoc.mpch-mainz.gwdg.de>) and our data from altered tephras (see  
113 Methods). Specifically, marine sediment-hosted tephras from the Lesser Antilles and the  
114 Aleutian arcs have been analysed and compared to similar data from eight additional modern  
115 volcanic provinces (Fig. 1). In addition to direct input of P from volcanic ash deposition, the  
116 emplacement and subsequent terrestrial weathering of extensive ash beds would have led to a  
117 secondary source of P to the oceans. The scale of this P flux has been estimated from a Monte  
118 Carlo simulation of inputs using published variables including the number, and scale of  
119 eruptions (Methods, Extended Data Figures 1, 2).

120 Depletion factors indicate between 31% (mean) and 48% (median) of the P originally  
121 hosted in tephra is lost during early diagenesis (Fig. 3). The potential scale of this process is  
122 calculated in the modern oceans, using an average of  $1.14 \pm 0.6 \text{ km}^3$  ash deposited per year,  
123 with  $70 \pm 7.5 \%$  falling into the ocean<sup>31</sup>, an ash density of  $1400 \pm 130 \text{ kg/m}^3$  (ref.<sup>32</sup>), and an  
124 original P content in tephra of  $0.41 \pm 0.19 \text{ wt}\%$  (ref.<sup>33</sup>). For each variable, a Monte Carlo-  
125 based approach is applied, using the average and standard deviation to develop 10,000  
126 possible iterations of each variable. From this calculation, the most likely annual P flux from

127 ash deposition and diagenesis is estimated to be approximately  $3 \times 10^{10}$  mol P yr<sup>-1</sup>. This is  
128 similar to estimates of global dust input to the P cycle today ( $3.2 \times 10^{10}$  mol P yr<sup>-1</sup>), and  
129 exceeds the dissolved riverine input ( $0.6 - 1.1 \times 10^{10}$  mol P yr<sup>-1</sup>; ref.<sup>34</sup>). Present-day volcanism  
130 is thought to be far smaller in scale than in periods such as the Ordovician<sup>35,36</sup>. Therefore,  
131 enhanced P supply tied to volcanism likely played an even more important role in  
132 biogeochemical cycles of P during the Ordovician.

### 133 **Impact of volcanic ash supply on Late Ordovician climate**

134 The depletion factors and estimates of ash supply during the Late Ordovician can be  
135 used to quantify the scale of P supply during the two studied events. For the GICE, our  
136 simulations indicate a mean of  $2.29 \times 10^{15}$  mol P (Fig. 4), which increases to  $6.49 \times 10^{15}$  mol  
137 P in the upper estimates of the simulations (95<sup>th</sup> percentile). For the volcanic episode covering  
138 the HICE, our simulations suggest a mean supply of  $2.89 \times 10^{15}$  mol P, with an upper estimate  
139 of  $8.24 \times 10^{15}$  mol P (95<sup>th</sup> percentile) (Fig. 4). In addition to ash falling into the ocean, the  
140 impact of erosion of terrestrially emplaced ash and lava on the P cycle is considered by  
141 estimating weathering fluxes of P (Methods). Newly emplaced ashes and basaltic rocks  
142 weather rapidly<sup>37,38</sup>, such that in Earth's modern configuration, despite representing only 3 –  
143 5% of land area, chemical weathering of basalt contributes ~30% of the total CO<sub>2</sub>  
144 consumption by silicate weathering<sup>37,38</sup>. Our approach to quantifying the impact of this  
145 process results in a mean additional (riverine) P flux from weathering of  $7.51 \times 10^{14}$  mol P  
146 Myr<sup>-1</sup> in the millennia after emplacement (Fig. 4c), with an upper estimate of  $1.23 \times 10^{15}$  mol  
147 P Myr<sup>-1</sup> (95<sup>th</sup> percentile), providing another source of bioavailable P to the ocean system.

148 The impact of this level of volcanic nutrient supply on Ordovician climate is estimated  
149 using the COPSE global biogeochemical model<sup>39</sup>. The GICE and HICE P inputs are  
150 represented by Gaussian functions with their maxima at the times of highest depositional  
151 intensity noted above (i.e., 453.5 and 444 Ma) and with a width of 2 Myrs, constrained in part

152 by the duration of the carbon isotope excursions. The total P input is calculated for both the  
153 means and 95<sup>th</sup> percentiles and is summed from the P depletion model and weathering inputs.  
154 A further factor is also added into the P delivery calculation to represent the recycling of P  
155 from sediments, because P loading and eutrophication in marginal settings leads to a  
156 substantial recycling flux of P from the sediments<sup>40</sup>, due to the increase in anaerobic  
157 processing of organic matter and the scarcity of Fe(III) phases that scavenge P. The COPSE  
158 model does not represent these feedbacks well, because it has a well-mixed global ocean and  
159 no consideration of continental margins, with substantial recycling of P relying on  
160 eutrophication of the global ocean rather than productive shelves and slope environments  
161 alone<sup>39</sup>. This is relevant to the Ordovician, a time when sea level was perhaps 300 m higher  
162 than present<sup>41</sup>, with extensive shelf environments<sup>42</sup>. Hence, parallel experiments were run to  
163 determine the degree to which P recycling is dampened in COPSE versus a published P cycle  
164 model in which the shelves are considered separately (see Methods, ref.<sup>43</sup>). We conclude that  
165 a 5-fold larger P input is required in COPSE to produce the same spike in marine P  
166 concentration observed in the multi-box model (Extended Data Figure 3). Thus, P inputs in  
167 the additional COPSE simulations are increased 5-fold to represent both the initial input and  
168 the additional recycling of P. The large size of this factor is related to the relatively small size  
169 of the ocean shelves (as a fraction of the whole ocean) compared to their disproportionately  
170 large contribution to organic matter burial.

171 An important parameter in COPSE is the degree to which land plants amplify  
172 continental weathering rates. This value is poorly constrained and is typically varied in  
173 sensitivity analyses between around 2- and 7-fold, giving a wide range of possible  
174 background CO<sub>2</sub> concentrations for the early Palaeozoic<sup>44</sup>. We choose a factor 2 enhancement  
175 for the model runs in this work, which gives a relatively low background Ordovician CO<sub>2</sub>  
176 concentration of around 1000 ppm, consistent with more recent proxy data<sup>45</sup>. Other than the  
177 new P inputs and choice of biotic weathering parameter, the model remains identical to the



178 long-term baseline shown in ref.<sup>39</sup>. Figure 5 shows the model outputs for atmospheric CO<sub>2</sub>,  
179 average surface temperature, marine anoxia, and the δ<sup>13</sup>C of new sedimentary carbonates. The  
180 model outputs show that the P release from volcanic ash deposition and weathering, combined  
181 with the recycling of P from sediments, is sufficient to cause large-scale changes in climate  
182 and biogeochemistry as observed in the geological record<sup>10,14</sup>. In the “95<sup>th</sup> percentile +  
183 recycling” input scenario, carbon isotope excursions of ~3‰ and ~4‰ are predicted, which  
184 are synchronous with the GICE and HICE, respectively, and are of similar magnitude. In this  
185 scenario, maximum global cooling at the HICE is around 3°C, and a global average surface  
186 temperature of below 15°C is reached at the nadir. These temperature predictions are in line  
187 with clumped isotope thermometry which suggests the Hirnantian icehouse was relatively  
188 short lived and represented a similar global average temperature to recent Pleistocene  
189 glaciation<sup>6,46</sup>.

190         The extent of marine anoxia increases during the P input events in the model, although  
191 given the global well-mixed ocean in the model, shelf anoxia would be expected to increase  
192 by a larger fraction than the global ocean. This is against a backdrop of marine oxygenation  
193 through the Ordovician and Silurian predicted by COPSE<sup>39</sup>. One of the major features of the  
194 HICE in the geological record is the widespread formation of organic-rich shales, in particular  
195 in China<sup>47,48</sup>, potentially linked to widespread ocean anoxia<sup>10,49</sup>. In COPSE, the relative  
196 increase in anoxia is much larger during the HICE – close to a doubling in the “95<sup>th</sup> percentile  
197 + recycling” scenario.

## 198 **Implications for the LOME**

199         Our model results suggest that volcanic ash diagenesis and weathering of erupted  
200 products likely played a key role in the Late Ordovician Earth system. In order to reproduce  
201 the magnitude of Earth system change, we require that these inputs are at the 95<sup>th</sup> percentile of  
202 our analysis. However, given the relatively sparse nature of the geological record of the

203 Palaeozoic, and the conservative approach utilised here to derive estimates of P supply from  
204 ash (Methods), we stress that our analysis likely underestimates the number of volcanic  
205 events. This is supported by the close comparison between the model output of the “95th  
206 percentile + recycling” input scenario and proxy data (Fig. 5, ref.<sup>50</sup>). Our results may explain  
207 several features of the LOME, which do not follow trends associated with other mass  
208 extinctions, in particular their link to cooling, rather than warming. Volcanic activity has been  
209 invoked as the driver behind a number of short-term climatic upheavals and mass  
210 extinctions<sup>51</sup>, including those at the end of the Permian<sup>52</sup> and in the Triassic periods<sup>53</sup>,  
211 resulting in the rapid fluctuations between icehouse and greenhouse conditions known to  
212 stress faunas and drive biodiversity loss<sup>3,52</sup>.

213 For the Late Ordovician, it appears that the long-term nature of nutrient supply from  
214 weathering of eruptive products such as volcanic ash plays a more dominant role than the  
215 medium-term warming associated with CO<sub>2</sub> injection. When comparing to climatic change, it  
216 is clear that the first stepped decrease in faunal diversity occurred soon after the GICE, with  
217 two further decreases occurring temporally close to the HICE<sup>3,54</sup>. Our approach considers  
218 many eruptions to estimate nutrient supply on a coarse scale. The super-eruptions represented  
219 by bentonites would likely have led to initial cooling (due to injection of stratospheric  
220 aerosols), followed by warming (from CO<sub>2</sub> injection), before cooling because of increases in  
221 nutrient supply and associated productivity levels. The warming/cooling cycles this scenario  
222 represents are purportedly dangerous for organisms, with biodiversity loss occurring when  
223 temperatures fall outside the optimal window<sup>3</sup>, potentially explaining the LOME initiation.  
224 Due to their global nature, we focus on the HICE and GICE, and only model two P pulses.  
225 However, bentonite ages suggest that multiple eruptions occurred between the two largest  
226 volcanic episodes and CIEs (Fig. 1), which may have led to transient local CIEs, such as those  
227 reported in the Scandinavian sections<sup>7</sup>.

228 In addition to releasing nutrients, it is possible that other toxic metals are also released  
229 during ash alteration and diagenesis<sup>25</sup>. During the Hirnantian glaciation and the HICE, there is  
230 evidence for metal-induced malformations in fossil plankton assemblages<sup>55</sup>. Further, volcanic  
231 ash may lead to the formation of large-scale anoxic conditions below deposited blankets<sup>24</sup>,  
232 which may have further enhanced redox-based recycling of toxic metals<sup>55</sup> and led to the  
233 deposition of widespread black shales<sup>47</sup>. Using the evidence presented here, we conclude that  
234 the pulsed nature of global cooling at this time appears to be a result of the eruption of two  
235 distinct volcanic provinces, one in what is now North America and the Baltic, and one in what  
236 is now Southern China. Further, our models suggest that the deposition of extensive ash  
237 blankets and weathering of lavas emplaced during Late Ordovician volcanism, supplied  
238 sufficient P to drive global cooling, glaciation, and the LOME.

### 239 **Acknowledgements**

240 This work was funded by NERC grant NE/K00543X/1, “The role of marine diagenesis of  
241 tephra in the carbon cycle”. B.J.W.M. acknowledges support from NERC grant  
242 NE/S009663/1. T.M.G. acknowledges support of NERC grant NE/R004978/1, and funding  
243 from the Alan

244 Turing Institute (EP/N510129/1). We are grateful for comments from Christian Rasmussen  
245 and the anonymous reviewer(s), which helped to improve the manuscript. We are grateful to  
246 staff of the IODP Gulf Coast Repository and IODP Kochi Core Repository for their assistance  
247 during sampling of cores U1396C and U1339D, respectively.

### 248 **Author Contributions**

249 J.L., T.M.G. and M.R.P. conceived this research. J.L. and H.R.M. completed the laboratory  
250 analyses. B.J.W.M. completing the modelling and J.L. compiled and analysed the data. J.L.

251 and B.J.W.M. created the figures. J.L. and B.J.W.M. wrote the manuscript, with input from  
252 T.M.G., H.R.M. and M.R.P.

### 253 **Competing Interests**

254 The authors declare no competing interests.

### 255 **Corresponding Author**

256 All correspondence and request for materials should be addressed to Jack Longman  
257 ([jack.longman@uni-oldenburg.de](mailto:jack.longman@uni-oldenburg.de))

### 258 **Figure Captions**

259 **Figure 1: Compilation of Late Ordovician bentonite ages from North America and**  
260 **China.** Bentonites ages in North America/Scandinavia (**a**), and China (**b**). Each age is  
261 represented by a probability density curve derived from published mean and standard  
262 deviation, from which 10,000 Monte Carlo simulations were completed and binned at 0.25  
263 Myr intervals to attain probability densities of the eruption occurring in each bin. Colours  
264 correspond to the studies from which each age is obtained. **c**, Average probability densities  
265 for each 0.25 Myr bin, for the North American (blue) and Chinese bentonites (red). Vertical  
266 lines indicate the bin in which bentonite deposition is most likely. (See Supplementary Tables  
267 4 and 5 for references).

268 **Figure 2: Paleogeographic reconstruction for the Late Ordovician at c. 450 Ma (Katian).**

269 Marked with ellipses are the two volcanic provinces investigated in this study, with blue  
270 ellipses representing the North American and Scandinavian province, and a green ellipse to  
271 represent the Chinese province. The base map was constructed using the plate tectonic  
272 reconstructions from ref.<sup>56</sup> and is based partly on ref<sup>57</sup>.

**Figure 3: Box and whisker diagrams of phosphorus depletion, an indicator of the amount of phosphorus lost to the ocean, from ten present-day representative volcanic provinces (a).** Boxes are defined between the

275 first and third quartile (the interquartile range, IQR), with minimum and maximum whiskers  
276 representative of 1.5 times the IQR. Also shown is a map of each volcanic province used for  
277 this reconstruction **(b)**, with the provinces identified by numbers given in panel **(a)**. **Figure 4:**  
278 **Monte Carlo simulations of phosphorus supply from volcanic weathering during the**  
279 **Late Ordovician, with variable distributions defined by our ash depletion and**  
280 **weathering model.** **(a)** and **(b)** represent P supply from ash deposition and diagenesis. In both  
281 panels, the total ash volume is presented along the x-axis, with total phosphorus supply on the  
282 y-axis. Each Monte Carlo simulation is indicated by a circle, with the colour indicating the  
283 depletion factor. **(c)** Estimate of P flux resulting from weathering of terrestrial volcanic matter  
284 (y-axis), plotted against the area covered by this ash and lava. Again, each simulation is  
285 indicated by a filled circle, with the colour denoting the rate of phosphorus supply.

286 **Figure 5. Biogeochemical model outputs for impacts of volcanism during the GICE and**  
287 **HICE.** COPSE model baseline runs<sup>39</sup> plus P supply from ash. **a**, Grey lines show the P input  
288 Gaussian functions (see text). The P input magnitude follows the mean or 95<sup>th</sup> percentiles of  
289 the values derived for ash supply and weathering combined, with or without recycling of P  
290 from sediments (see main text). **b**, Modelled  $\delta^{13}\text{C}$  of carbonates (with colours defined in panel  
291 e) compared to data<sup>50</sup> (yellow circles). **c**, Modelled atmospheric  $\text{CO}_2$ . **d**, Modelled global  
292 average surface temperature. **e**, Degree of marine anoxia (represented as the modelled  
293 proportion of anoxic seafloor). Solid lines show the same simulations as the dashed lines, but  
294 with additional P input to represent sedimentary recycling of P (see text).

## 295 **References**

- 296 1. Harper, D. A. T., Hammarlund, E. U. & Rasmussen, C. M. Ø. End Ordovician extinctions: A  
297 coincidence of causes. *Gondwana Res.* 25, 1294–1307 (2014).
- 298 2. Bambach, R. K., Knoll, A. H. & Wang, S. C. Origination, extinction, and mass depletions of  
299 marine diversity. *Paleobiology* 30, 522–542 (2004).

- 300 3. Rasmussen, C. M. Ø., Kröger, B., Nielsen, M. L. & Colmenar, J. Cascading trend of Early  
301 Paleozoic marine radiations paused by Late Ordovician extinctions. *Proc. Natl. Acad. Sci. U. S. A.*  
302 116, 7207–7213 (2019).
- 303 4. Bergström, S. M., Schmitz, B., Saltzman, M. R. & Huff, W. D. The Upper Ordovician  
304 Guttenberg  $\delta^{13}\text{C}$  excursion (GICE) in North America and Baltoscandia: Occurrence,  
305 chronostratigraphic significance, and paleoenvironmental relationships. *Geol. Soc. Am. Spec. Pap.*  
306 466, 37–67 (2010).
- 307 5. Metzger, J. G., Ramezani, J., Bowring, S. A. & Fike, D. A. New age constraints on the  
308 duration and origin of the Late Ordovician Guttenberg  $\delta^{13}\text{C}_{\text{carb}}$  excursion from high-precision U-Pb  
309 geochronology of K-bentonites. *GSA Bull.* (2020) doi:10.1130/B35688.1.
- 310 6. Finnegan, S. et al. The magnitude and duration of late Ordovician-early Silurian glaciation.  
311 *Science*. 331, 903–906 (2011).
- 312 7. Ainsaar, L. et al. Middle and Upper Ordovician carbon isotope chemostratigraphy in  
313 Baltoscandia: A correlation standard and clues to environmental history. *Palaeogeogr. Palaeoclimatol.*  
314 *Palaeoecol.* 294, 189–201 (2010).
- 315 8. Lenton, T. M., Crouch, M., Johnson, M., Pires, N. & Dolan, L. First plants cooled the  
316 Ordovician. *Nat. Geosci.* 5, 86–89 (2012).
- 317 9. Mills, B. J. W. et al. Modelling the long-term carbon cycle, atmospheric  $\text{CO}_2$ , and Earth  
318 surface temperature from late Neoproterozoic to present day. *Gondwana Research* vol. 67 172–186  
319 (2019).
- 320 10. Shen, J. et al. Improved efficiency of the biological pump as a trigger for the Late Ordovician  
321 glaciation. *Nat. Geosci.* 11, 510–514 (2018).
- 322 11. Swanson-Hysell, N. L. & Macdonald, F. A. Tropical weathering of the Taconic orogeny as a  
323 driver for Ordovician cooling. *Geology* 45, 719–722 (2017).

- 324 12. Bartlett, R. et al. Abrupt global-ocean anoxia during the Late Ordovician–early Silurian  
325 detected using uranium isotopes of marine carbonates. *Proc. Natl. Acad. Sci. U. S. A.* 115, 5896–5901  
326 (2018).
- 327 13. Morris, J. L. et al. The timescale of early land plant evolution. *Proc. Natl. Acad. Sci. U. S. A.*  
328 115, E2274–E2283 (2018).
- 329 14. Buggisch, W. et al. Did intense volcanism trigger the first Late Ordovician icehouse? *Geology*  
330 38, 327–330 (2010).
- 331 15. Herrmann, A. D., Leslie, S. A. & MacLeod, K. G. Did intense volcanism trigger the first Late  
332 Ordovician icehouse?: COMMENT. *Geology* 39, e237–e237 (2011).
- 333 16. Huff, W. D., Bergström, S. M. & Kolata, D. R. Ordovician explosive volcanism. *Geol. Soc.*  
334 *Am. Spec. Pap.* 466, 13–28 (2010).
- 335 17. Tao, H., Qiu, Z., Lu, B., Liu, Y. & Qiu, J. Volcanic activities triggered the first global cooling  
336 event in the Phanerozoic. *J. Asian Earth Sci.* 104074 (2019) doi:10.1016/j.jseas.2019.104074.
- 337 18. Huff, W. D., Kolata, D. R., Bergström, S. M. & Zhang, Y. S. Large-magnitude Middle  
338 Ordovician volcanic ash falls in North America and Europe: Dimensions, emplacement and post-  
339 emplacement characteristics. *J. Volcanol. Geotherm. Res.* 73, 285–301 (1996).
- 340 19. Sell, B. K. et al. Stratigraphic correlations using trace elements in apatite from late Ordovician  
341 (Sandbian-Katian) K-bentonites of eastern North America. *Bull. Geol. Soc. Am.* 127, 1259–1274  
342 (2015).
- 343 20. Ballo, E. G., Augland, L. E., Hammer, Ø. & Svensen, H. H. A new age model for the  
344 Ordovician (Sandbian) K-bentonites in Oslo, Norway. *Palaeogeogr. Palaeoclimatol. Palaeoecol.* 520,  
345 203–213 (2019).
- 346 21. Liu, W. et al. K-bentonites in Ordovician-Silurian transition from South China: Implications  
347 for tectonic evolution in the northern margin of Gondwana. *J. Geol. Soc. London.* jgs2020-049 (2020)  
348 doi:10.1144/jgs2020-049.

- 349 22. Smolarek-Lach, J., Marynowski, L., Trela, W. & Wignall, P. B. Mercury Spikes Indicate a  
350 Volcanic Trigger for the Late Ordovician Mass Extinction Event: An Example from a Deep Shelf of  
351 the Peri-Baltic Region. *Sci. Rep.* 9, 1–11 (2019).
- 352 23. Jones, D. S., Martini, A. M., Fike, D. A. & Kaiho, K. A volcanic trigger for the late  
353 Ordovician mass extinction? Mercury data from south China and Laurentia. *Geology* 45, 631–634  
354 (2017).
- 355 24. Longman, J., Palmer, M. R., Gernon, T. M. & Manners, H. R. The role of tephra in enhancing  
356 organic carbon preservation in marine sediments. *Earth-Science Rev.* 192, 480–490 (2019).
- 357 25. Jones, M. T. & Gislason, S. R. Rapid releases of metal salts and nutrients following the  
358 deposition of volcanic ash into aqueous environments. *Geochim. Cosmochim. Acta* 72, 3661–3680  
359 (2008).
- 360 26. Sell, B., Ainsaar, L. & Leslie, S. Precise timing of the Late Ordovician (Sandbian) super-  
361 eruptions and associated environmental, biological, and climatological events. *J. Geol. Soc. London.*  
362 170, 711–714 (2013).
- 363 27. Tucker, R. D. & McKerrow, W. S. Early Paleozoic chronology: a review in light of new U-Pb  
364 zircon ages from Newfoundland and Britain. *Can. J. Earth Sci.* 32, 368–379 (1995).
- 365 28. Ling, M. X. et al. An extremely brief end Ordovician mass extinction linked to abrupt onset of  
366 glaciation. *Solid Earth Sci.* 4, 190–198 (2019).
- 367 29. Du, X. et al. Was volcanic activity during the Ordovician-Silurian transition in South China  
368 part of a global phenomenon? Constraints from zircon U–Pb dating of volcanic ash beds in black  
369 shales. *Mar. Pet. Geol.* 114, 104209 (2020).
- 370 30. Lee, C.-T. A. et al. Volcanic ash as a driver of enhanced organic carbon burial in the  
371 Cretaceous. *Sci. Rep.* 8, 4197 (2018).
- 372 31. Longman, J., Palmer, M. R., Gernon, T. M. & Manners, H. R. Subaerial volcanism is a major  
373 contributor to oceanic iron and manganese cycles. In Review.



- 374 32. Gudmundsson, M. T. et al. Ash generation and distribution from the April-May 2010 eruption  
375 of Eyjafjallajökull, Iceland. *Sci. Rep.* 2, 572 (2012).
- 376 33. Laeger, K. et al. High-resolution geochemistry of volcanic ash highlights complex magma  
377 dynamics during the Eyjafjallajökull 2010 eruption. *Am. Mineral.* 102, 1173–1186 (2017).
- 378 34. Paytan, A. & McLaughlin, K. The oceanic phosphorus cycle. *Chem. Rev.* 107, 563–576  
379 (2007).
- 380 35. Cao, W., Lee, C. T. A. & Lackey, J. S. Episodic nature of continental arc activity since 750  
381 Ma: A global compilation. *Earth Planet. Sci. Lett.* 461, 85–95 (2017).
- 382 36. Mills, B. J. W., Scotese, C. R., Walding, N. G., Shields, G. A. & Lenton, T. M. Elevated CO<sub>2</sub>  
383 degassing rates prevented the return of Snowball Earth during the Phanerozoic. *Nat. Commun.* 8, 1–7  
384 (2017).
- 385 37. Dessert, C., Dupré, B., Gaillardet, J., François, L. M. & Allègre, C. J. Basalt weathering laws  
386 and the impact of basalt weathering on the global carbon cycle. *Chem. Geol.* 202, 257–273 (2003).
- 387 38. Dessert, C. et al. Erosion of Deccan Traps determined by river geochemistry: impact on the  
388 global climate and the <sup>87</sup>Sr/<sup>86</sup>Sr ratio of seawater. *Earth Planet. Sci. Lett.* 188, 459–474 (2001).
- 389 39. Tostevin, R. & Mills, B. J. W. Reconciling proxy records and models of Earth’s oxygenation  
390 during the Neoproterozoic and Palaeozoic. *Interface Focus* 10, 20190137 (2020).
- 391 40. Slomp, C. P. & Van Cappellen, P. The global marine phosphorus cycle: sensitivity to oceanic  
392 circulation. *Biogeosciences* 4, 155–171 (2007).
- 393 41. Hallam, A. *Phanerozoic sea-level changes.* (Columbia Univeristy Press, 1992).
- 394 42. Walker, L. J., Wilkinson, B. H. & Ivany, L. C. Continental drift and phanerozoic carbonate  
395 accumulation in shallow-shelf and deep-marine settings. *J. Geol.* 110, 75–87 (2002).
- 396 43. Alcott, L. J., Mills, B. J. W. & Poulton, S. W. Stepwise Earth oxygenation is an inherent  
397 property of global biogeochemical cycling. *Science* . 366, 1333–1337 (2019).

- 398 44. Berner, R. A. A model for atmospheric CO<sub>2</sub> over Phanerozoic time. *Am. J. Sci.* 291, 339–376  
399 (1991).
- 400 45. Witkowski, C. R., Weijers, J. W. H., Blais, B., Schouten, S. & Sinninghe Damsté, J. S.  
401 Molecular fossils from phytoplankton reveal secular PCO<sub>2</sub> trend over the phanerozoic. *Sci. Adv.* 4,  
402 eaat4556 (2018).
- 403 46. Goldberg, S. L., Present, T. M., Finnegan, S. & Bergmann, K. D. A high-resolution record of  
404 early Paleozoic climate. *Proc. Natl. Acad. Sci.* 118, (2021).
- 405 47. Zou, C. et al. Organic-matter-rich shales of China. *Earth-Science Reviews* vol. 189 51–78  
406 (2019).
- 407 48. Su, W. et al. K-bentonite, black-shale and flysch successions at the Ordovician-Silurian  
408 transition, South China: Possible sedimentary responses to the accretion of Cathaysia to the Yangtze  
409 Block and its implications for the evolution of Gondwana. *Gondwana Res.* 15, 111–130 (2009).
- 410 49. LaPorte, D. F. et al. Local and global perspectives on carbon and nitrogen cycling during the  
411 Hirnantian glaciation. *Palaeogeogr. Palaeoclimatol. Palaeoecol.* 276, 182–195 (2009).
- 412 50. Saltzman, M. R. & Thomas, E. Carbon isotope stratigraphy. in *The Geologic Time Scale 2012*  
413 (eds. Gradstein, F. M., Ogg, J., Schmitz, M. D. & Ogg, G, M.) 207–232 (Elsevier, 2012).  
414 doi:10.1016/B978-0-444-59425-9.00011-1.
- 415 51. Sobolev, S. V. et al. Linking mantle plumes, large igneous provinces and environmental  
416 catastrophes. *Nature* 477, 312–316 (2011).
- 417 52. Black, B. A. et al. Systemic swings in end-Permian climate from Siberian Traps carbon and  
418 sulfur outgassing. *Nat. Geosci.* 11, 949–954 (2018).
- 419 53. Schoene, B., Guex, J., Bartolini, A., Schaltegger, U. & Blackburn, T. J. Correlating the end-  
420 Triassic mass extinction and flood basalt volcanism at the 100 ka level. *Geology* 38, 387–390 (2010).
- 421 54. Fan, J. X. et al. A high-resolution summary of Cambrian to early Triassic marine invertebrate  
422 biodiversity. *Science* . 367, 272–277 (2020).

423 55. Vandenbroucke, T. R. A. et al. Metal-induced malformations in early Palaeozoic plankton are  
424 harbingers of mass extinction. *Nat. Commun.* 6, (2015).

425 56. Meredith, A. S. et al. Extending full-plate tectonic models into deep time: Linking the  
426 Neoproterozoic and the Phanerozoic. *Earth-Science Rev.* 214, 103477 (2021).

427 57. Cocks, L. R. M. & Torsvik, T. H. Ordovician palaeogeography and climate change.  
428 *Gondwana Res.* (2020) doi:10.1016/j.gr.2020.09.008.

429

## 430 **Methods**

### 431 **Major and trace element geochemistry**

432 Tephra layers from IODP cores 1396C (Lesser Antilles) and U1339D (Bering Sea)  
433 were analysed for their phosphorus content. Tephrae were identified visually, and  
434 microscopically, in core 1339D and through their low CaCO<sub>3</sub> content in U1396C. P was  
435 analysed in tephra layers after mixed acid (HNO<sub>3</sub>-HCl-HF) bench-top digestion. Samples  
436 were then analysed on a Perkin Elmer 2000B at the University of Oxford. Analysis was  
437 completed in both standard mode (m/z 31) and in reaction mode, with O<sub>2</sub> as reaction gas and  
438 analysis on m/z 47. In all cases, data were more accurate and detection limits were sufficient  
439 from standard mode analysis and so we present these results here. Blanks and standards  
440 (BHVO2 basalt) were prepared and analysed in the same manner (Supplementary Table 1).  
441 For cores U1396C and U1339D, Al and Zr were determined after digestion using the same  
442 procedure as above, again alongside standard BHVO2 and blanks. Concentrations of these  
443 elements were determined using a Thermo X-Series ICP-MS at the University of  
444 Southampton (Supplementary Table 1).

### 445 **P depletion factors and P release**

446 We used the GEOROC database to estimate the protolith composition of volcanic  
447 material from each of the source regions. These data were filtered to remove any data related

448 to non-outcrop samples, xenoliths and any mineral-specific analyses. This database was used  
 449 to estimate the composition of tephra prior to dissolution and diagenetic alteration. By  
 450 normalising P to Zr and plotting this ratio against Ti/Zr (elements which are largely immobile  
 451 during diagenesis), the empirical relationship between the two ratios can be used to estimate  
 452 the original protolith composition following the method of ref.<sup>30</sup>, developed to estimate metal  
 453 mobility in Cretaceous tephra (Supplementary Table 2). The linear regression representing  
 454 this relationship is then used back-calculate the original composition of altered tephra  
 455 (Supplementary Tables 2, 3, refs.<sup>58-64</sup>). These compositions, along with compositions of  
 456 altered tephra, are then used to calculate depletion factors using the following equation  
 457 (Equation 1):

$$P_D = \frac{M_P^L}{M_P^O} = 1 - \frac{\left(\frac{C_P^{re}}{C_{Zr}^{re}}\right)}{\left(\frac{C_P^O}{C_{Zr}^O}\right)} \text{ (Eq. 1)}$$

458 The left side of the equation is the depletion factor, where  $M_P^O$  original P mass in the protolith,  
 459  $M_P^L$  is the loss of P.  $C_P^{re}$  and  $C_{Zr}^{re}$  are the mass of P and Zr in tephra, and  $C_P^O / C_{Zr}^O$  represents the  
 460 ratio of P to Zr in the protolith, back-calculated from the linear regression of GEOROC data  
 461 (Fig. 3, Extended Data Figures 1, 2).

## 462 **Estimating the extent and timing of volcanism during the Late Ordovician**

463 We use Monte Carlo simulations of variables associated with bentonite deposition  
 464 during the Late Ordovician to estimate the size of the volcanic eruptions and associated ash  
 465 deposition<sup>57</sup>. For the GICE period, we use values from published compilations of North  
 466 American bentonites<sup>5,19</sup> (Supplementary Table 4), and for the HICE we collate ages from  
 467 published bentonites from China (Supplementary Table 5). For the period 455 – 450 Ma  
 468 (corresponding to period covering the GICE), we take the number of ash layers to be 100  
 469 based on observations<sup>19</sup>. We assume these ash layers represent eruptions of VEI 8 due to the

470 location and characteristics of these bentonites, which constitute discrete centimetre-thick  
471 horizons thousands of kilometres from any proposed source<sup>16,19</sup>. We assume each eruption  
472 contained on average 1000 km<sup>3</sup> erupted material<sup>18</sup>. To estimate how much erupted material  
473 was ash, we use a value of 50%, representing the likely proportions in Ultraplinian  
474 eruptions<sup>18,21</sup>. Since we are only interested, in the first instance, in the ash which may directly  
475 supply P to the ocean, we use an estimate of 50% ashfall in the ocean basins. This number is  
476 based upon estimates of ashfall which has been subducted since the Ordovician, using  
477 isopachs constructed from North American outcrops<sup>18</sup>, and paleogeographic reconstructions  
478 which indicate volcanism was linked to the opening of the Iapetus Ocean (Figure 2). For all  
479 variables used in equation 2, we apply standard deviations of all variables set at 25% of the  
480 variable mean, unless stated (Supplementary Table 6). 10,000 simulations of all variables  
481 were performed using the r package *rtrucnorm*, and outputs were used to reconstruct likely  
482 ash volumes (in km<sup>3</sup>).

483 For the period 450 – 440 Ma (corresponding to period covering the HICE), a similar  
484 set of likely values for variables was constructed using published data on Chinese bentonite  
485 deposits<sup>21</sup>. In this case, we use 88 ash layers as our mean, derived from the subtraction of 16  
486 Silurian ashes from a compilation of Late Ordovician–early Silurian Chinese bentonites<sup>21,65</sup>.  
487 We use 75% as the oceanic fraction because this volcanism was linked with subduction of the  
488 Zhenge-Dapu Ocean (Figure 2), and so a high proportion will be deposited in this  
489 environment<sup>21</sup>. Again, we apply standard deviations of 25% to each of these variables to  
490 consider the uncertainty.

491 In both cases, to estimate ash density, and the amount of P contained in the original  
492 ashes, we use measured values from Icelandic ashfall<sup>32,33</sup>, with standard deviations derived  
493 from the measurements. Using the ash volume estimates derived from these variables, and our

494 depletion factors, we simulate 10,000 iterations for total P supply for each period (in mole P),  
495 using the following equation (Eq. 2):

496 
$$P \text{ release (mole)} = \left( \frac{V_{Ash} \times \rho_{Ash} \times P_{Ash} \times P_D}{30.97} \right) \times P_{ocean} \text{ (Equation 2)}$$

497 where  $V_{Ash}$ ,  $\rho_{Ash}$  and  $P_{Ash}$  are the volume of ash (in  $\text{km}^3$ ), density of ash (in  $\text{kg/m}^3$ ) and  
498 phosphorus content in ash (in wt %).  $P_D$  is the depletion factor of phosphorus,  $P_{ocean}$  is the  
499 proportion falling into the ocean and 30.97 is the molecular weight of P, to convert from  
500 grams to moles. Such an exercise provides an absolute amount of P released for each period,  
501 but for modelling purposes, we must convert our total P supply values into flux (in  $\text{mol P myr}^{-1}$ ).  
502 <sup>1</sup>).

503 To do this, we develop a dataset of all reliably dated (i.e., excluding K-Ar or fission  
504 track dates) bentonites of Late Ordovician age from across the two primary volcanic  
505 provinces, China and North America/Baltica (Figure 2, refs. <sup>5,20,21,26–29,65–80</sup>). For each of the  
506 dates, we use a Monte Carlo based approach to generate 10,000 possible ages, constrained by  
507 published age and error values. We group the outputs of this exercise into 0.25 Myr bins and  
508 produce probability density estimates for each bin (Fig. 1a, b). For each of the two volcanic  
509 provinces, we average across each bin to result in a probability density of each 0.25 Myr  
510 period (Fig. 1c). This exercise results in two distinct peaks, representing the most likely  
511 period of volcanism for both provinces. For North America/Scandinavia, this peak is centred  
512 on 453.5 Ma. For China, the volcanic peak occurs 444.0 Ma. To represent these events in the  
513 model we then use a standard Gaussian curve with  $\sigma=0.4$ , giving an event duration of around  
514 2 Myrs. This width is informed by the duration of the carbon isotope excursions.

### 515 **Estimating P flux from weathering**

516 We estimate the spatial extent of erupted material during the Late Ordovician using an  
517 averaged value from a modelling study of Ordovician volcanism ( $1.56 \times 10^6 \text{ km}^2$ ; ref.<sup>60</sup>). We

518 then use P release value of 29.77 kg P km<sup>-2</sup> yr<sup>-1</sup> as measured from basalts<sup>82</sup>. We estimate that  
519 50% of the ash and lava was terrestrially emplaced based on the observations of ash  
520 deposition considered previously<sup>18,21</sup>. By applying 20% errors to all of these values, we then  
521 carried out 10,000 Monte Carlo simulations of each variable, before calculating the final flux  
522 (in mol P myr<sup>-1</sup>) by multiplying each iteration of each variable.

### 523 **Biogeochemical modelling**

524 We use the latest COPSE biogeochemical model<sup>39</sup>. We run the model baseline and add  
525  $P_{force}$  to the global bioavailable phosphorus weathering flux (Equation 3). This adds additional  
526 phosphorus input during the Late Ordovician to the baseline model run.

$$527 P_{force} = 10^{-6} P_{GICE} \frac{norm(t, -453.45, 0.4)}{norm(-453.45, -453.45, 0.4)} + 10^{-6} P_{HICE} \frac{norm(t, -444, 0.4)}{norm(-444, -444, 0.4)} \text{ (Eq. 3)}$$

528 Here  $P_{GICE}$  and  $P_{HICE}$  are the total P inputs from ash, weathering, and recycling in moles. Here  
529  $norm$  is a normal function defined as  $norm(time, midpoint, \sigma)$ .  $P_{force}$  is multiplied by 5 in some  
530 simulations to represent the additional recycling of P which is not captured in the COPSE  
531 model. This factor is determined by running a P-C cycling model which has an explicit  
532 representation of the shelf<sup>43</sup> and comparing the ratio between P input from weathering and  
533 overall marine P concentration versus the same metric in COPSE. The reader is referred to  
534 Extended Data Figure 3 for the model comparison plots.

### 535 **Data Availability**

536 The authors declare that data supporting the findings of this study are available within the  
537 article and Supplementary Information and Extended Data. All data have also been uploaded  
538 to Figshare, at the following DOI addresses: <http://dx.doi.org/10.6084/m9.figshare.14914893>,  
539 <http://dx.doi.org/10.6084/m9.figshare.14914911>,  
540 <http://dx.doi.org/10.6084/m9.figshare.14914896> and  
541 <http://dx.doi.org/10.6084/m9.figshare.14914890>.

542 **Code availability**

543 COPSE model code can be downloaded at <https://github.com/bjwmills>

544 **Methods-only References**

545 58. Bitschene, P. R., Mehl, K. W. & Schmincke, H.-U. Composition and origin of marine ash  
546 layers and epiclastic rocks from the Kerguelen Plateau, southern Indian Ocean (Legs 119 and 120).  
547 Proc. Ocean Drill. Program, 120 Sci. Results 120, 135–149 (1992).

548 59. Schindlbeck, J. C. et al. One Million Years tephra record at IODP Sites U1436 and U1437:  
549 Insights into explosive volcanism from the Japan and Izu arcs. *Isl. Arc* 27, e12244 (2018).

550 60. Rodehorst, U., Schmincke, H.-U. & Sumita, M. Geochemistry and petrology of Pleistocene  
551 ash layers erupted at Las Cañadas Edifice (Tenerife). *Scientific Results* vol. 157 (1998).

552 61. Salisbury, M. J. et al. Deep-sea ash layers reveal evidence for large, late Pleistocene and  
553 Holocene explosive activity from Sumatra, Indonesia. *J. Volcanol. Geotherm. Res.* 231–232, 61–71  
554 (2012).

555 62. Derkachev, A. N. et al. Tephra layers of in the quaternary deposits of the Sea of Okhotsk:  
556 Distribution, composition, age and volcanic sources. *Quat. Int.* 425, 248–272 (2016).

557 63. Schindlbeck, J. C. et al. Late Cenozoic tephrostratigraphy offshore the southern Central  
558 American Volcanic Arc: 1. Tephra ages and provenance. *Geochemistry, Geophys. Geosystems* 17,  
559 4641–4668 (2016).

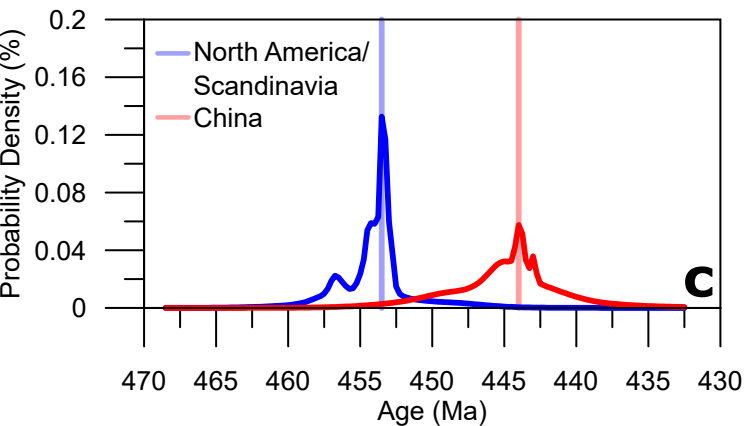
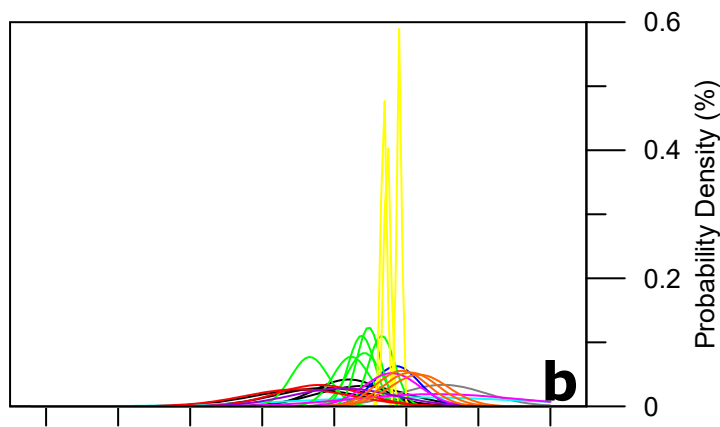
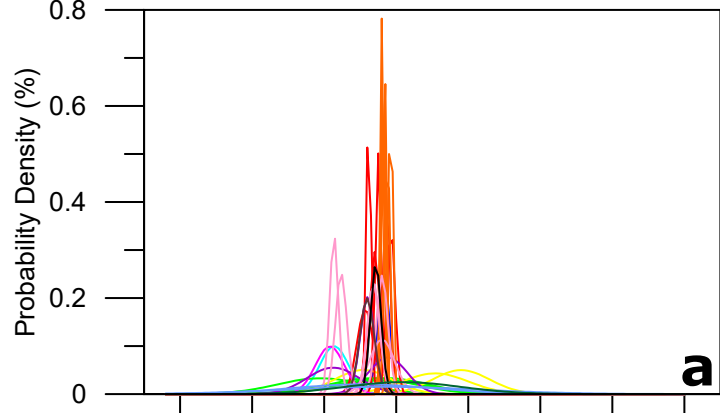
560 64. Allan, A. S. R., Baker, J. A., Carter, L. & Wysoczanski, R. J. Reconstructing the Quaternary  
561 evolution of the world's most active silicic volcanic system: insights from an ~1.65 Ma deep ocean  
562 tephra record sourced from Taupo Volcanic Zone, New Zealand. *Quat. Sci. Rev.* 27, 2341–2360  
563 (2008).

564 65. Yang, S. et al. Duration, evolution, and implications of volcanic activity across the  
565 Ordovician–Silurian transition in the Lower Yangtze region, South China. *Earth Planet. Sci. Lett.* 518,  
566 13–25 (2019).



- 567 66. Tucker, R. D. U-Pb dating of Plinian-eruption ashfalls by the isotopic dilution method: a  
568 reliable and precise tool for time-scale calibration and biostratigraphic correlation. *Geol. Soc. Amer.*  
569 *Abs. w/ Prog.* 24, A192 (1992).
- 570 67. Oruche, N. E., Dix, G. R. & Kamo, S. L. Lithostratigraphy of the upper Turinian – Lower  
571 Chatfieldian (upper Ordovician) foreland succession, and a U–Pb ID–TIMS date for the Millbrig  
572 volcanic ash bed in the Ottawa embayment. *Can. J. Earth Sci.* 55, 1079–1102 (2018).
- 573 68. Min, K., Renne, P. R. & Huff, W. D. Ar/Ar dating of Ordovician K-bentonites in Laurentia  
574 and Baltoscandia. *Earth Planet. Sci. Lett.* 185, 121–134 (2001).
- 575 69. Samson, S. D., Patchett, P. J., Roddick, J. C. & Parrish, R. R. Origin and tectonic setting of  
576 Ordovician bentonites in North America: isotopic and age constraints. *Geol. Soc. Am. Bull.* 101,  
577 1175–1181 (1989).
- 578 70. Svensen, H. H., Hammer, Ø. & Corfu, F. Astronomically forced cyclicity in the Upper  
579 Ordovician and U-Pb ages of interlayered tephra, Oslo Region, Norway. *Palaeogeogr. Palaeoclimatol.*  
580 *Palaeoecol.* 418, 150–159 (2015).
- 581 71. Bauert, H. et al. New U-Pb zircon ages of the Sandbian (Upper Ordovician) ‘Big K-bentonite’  
582 in Baltoscandia (Estonia and Sweden) by LA-ICPMS. *GFF* 136, 30–33 (2014).
- 583 72. Compston, W. & Williams, I. S. Ion probe ages for the British Ordovician and Silurian  
584 stratotypes. in *Global perspectives on Ordovician geology* (eds. Webby, B. D. & Laurie, J. R.) 59–67  
585 (1992).
- 586 73. Li, Y., Zhang, T., Shao, D. & Shen, B. New U-Pb zircon age and carbon isotope records from  
587 the Lower Silurian Longmaxi Formation on the Yangtze Platform, South China: Implications for  
588 stratigraphic correlation and environmental change. *Chem. Geol.* 509, 249–260 (2019).
- 589 74. Hu, Y. H., Zhou, J. Bin, Song, B., Li, W. & Sun, W. D. SHRIMP zircon U-Pb dating from K-  
590 bentonite in the top of Ordovician of Wangjiawan section, Yichang, Hubei, China. *Sci. China, Ser. D*  
591 *Earth Sci.* 51, 493–498 (2008).

- 592 75. Xie, S., Wang, Z., Wang, J. & Zhuo, J. LA-ICP-MS zircon U-Pb dating of the bentonites from  
593 the uppermost part of the Ordovician Wufeng Formation in the Haoping section, Taoyuan, Hunan.  
594 *Sediment. Tethyan Geol.* 4, 597 (2012).
- 595 76. Yang, S. et al. Constraints on the accumulation of organic matter in Upper Ordovician-lower  
596 Silurian black shales from the Lower Yangtze region, South China. *Mar. Pet. Geol.* 120, 104544  
597 (2020).
- 598 77. Ge, X. et al. Mineralogical and geochemical characteristics of K-bentonites from the Late  
599 Ordovician to the Early Silurian in South China and their geological significance. *Geol. J.* 54, 514–528  
600 (2019).
- 601 78. Zheng, B. et al. Nature of the Late Ordovician-Early Silurian Xiaohe section, Hunan-Hubei  
602 area, South China: implications for the Kwangsi Orogeny. *Int. Geol. Rev.* 62, 1262–1272 (2020).
- 603 79. Kunk, M. J., Sutter, J., Obradovich, J. D. & Lanphere, M. A. Age of biostratigraphic horizons  
604 within the Ordovician and Silurian systems. *Geol. Soc. Mem.* 10, 89–92 (1985).
- 605 80. Tucker, R. D., Krogh, T. E., Ross, R. J. & Williams, S. H. Time-scale calibration by high-  
606 precision UPb zircon dating of interstratified volcanic ashes in the Ordovician and Lower Silurian  
607 stratotypes of Britain. *Earth Planet. Sci. Lett.* 100, 51–58 (1990).
- 608 81. Lefebvre, V., Servais, T., François, L. & Averbuch, O. Did a Katian large igneous province  
609 trigger the Late Ordovician glaciation?. A hypothesis tested with a carbon cycle model. *Palaeogeogr.*  
610 *Palaeoclimatol. Palaeoecol.* 296, 310–319 (2010).
- 611 82. Hartmann, J., Moosdorf, N., Lauerwald, R., Hinderer, M. & West, A. J. Global chemical  
612 weathering and associated p-release - the role of lithology, temperature and soil properties. *Chem.*  
613 *Geol.* 363, 145–163 (2014).



450 Ma

